

STUDY OF RADIATIVE ELECTRON CAPTURE IN
RELATIVISTIC ION-ATOM COLLISIONS

by
Hao Ding

Thesis Submitted in Partial Fulfillment
of the Requirements for the Degree of
M. Sc. in Photonics

in the
Abbe School of Photonics
Friedrich-Schiller-Universität Jena
Physikalisch-Astronomische Fakultät

Advisors: Prof. Dr. Thomas Stöhlker
Dr. Günter Weber

Referees: Prof. Dr. Thomas Stöhlker
Prof. Dr. Malte C. Kaluza

Date of thesis defence:

Location:

Contents

1	Introduction	1
2	Physics Background	5
2.1	Basic Concepts	5
2.1.1	Cross Section	5
2.1.2	Four-vector	7
2.1.3	Lorentz Transformation	7
2.1.4	Polarization of Photons	9
2.2	Hard X-ray Interacting with Matter	11
2.2.1	Photon Absorption	11
2.2.2	Photon Scattering	14
2.3	Compton Polarimetry	16
3	Theoretical Description of REC	20
3.1	Impulse Approximation	21
3.1.1	Validity of Impulse Approximation	25
3.2	Radiative Recombination I: Approximate Methods	26
3.2.1	Photoelectric Effect	26
3.2.2	Born Approximation	27
3.2.3	Stobbe Formula	30
3.3	Radiative Recombination II: Density Matrix Theory	31
4	Experimental Study of REC	36
4.1	Instrumentation – GSI	36
4.1.1	Heavy Ion Accelerators	36
4.1.2	Experimental Storage Ring	38
4.1.3	Internal Jet-Target	41

4.2	Experimental Setup	43
4.2.1	Si(Li) Polarimeter	44
5	Outcomes of Study	46
5.1	Calculator for REC Cross Section and Polarization	46
5.1.1	Database of Elements	47
5.1.2	Interpolation Procedure	48
5.1.3	Accuracy of Interpolation	49
5.2	Linear Polarization of REC Photons	51
5.2.1	X-ray Spectrum	51
5.2.2	Linear Polarization	56
5.2.3	Monte Carlo Simulation	59
5.2.4	Comparison between Experimental Results and Theory	62
6	Additional Experimental Work	64
7	Summary and Outlook	68
	Bibliography	70

1 Introduction

Collisions of highly-charged heavy ions with neutral targets at relativistic energies have been extensively studied during the last decades in both accelerators and storage ring facilities [1–4], which have provided non-precedent understandings of the atomic structures and the dynamics of basic interaction processes.

In such collisions, especially when few-electron or even bare projectile ions are utilized, many possible kinds of basic interactions may occur. Particularly, detailed studies of the amongst simple and confined ones such as radiative electron capture (REC) [5, 6], Lyman- [7, 8], Balmer- [9], and intra-shell transitions [10], as well as the Bremsstrahlung process in inverse kinematics [11, 12] were carried out by the atomic physics division of the GSI Helmholtzzentrum für Schwerionenforschung. The present master thesis is dedicated to study the first above-mentioned process: the radiative electron capture of a bound target electron into a bound state of a fast projectile.

The general form of the capture of an electron by a projectile ion, P^{q+} (of atomic number Z_P and charge state $q+$), from a target atom, T (of atomic number Z_T), can be schematically described by



In the non-relativistic energy regime, the cross section¹ for this (non-radiative) process falls off asymptotically as v^{-12} [13] with v being the projectile velocity, due to the requirement for momentum match.²

However, this stringent momentum condition leading to the rapid decrease can be loosen by accompanying the capture process with the emission of a photon to carry

¹The “cross section” is a measure for the probability of interaction (c.f. subsection 2.1.1).

²The initial momentum has to find, for each of its components, a counterpart in the final momentum wave function that is displaced by $m_e \mathbf{v}$ (the momentum of an electron traveling with the velocity of the projectile). With increasing displacement, the overlap of the tails of the two momentum distributions will rapidly decrease, especially for the collisions between low- Z ions (atoms).

away the energy and momentum excess:



Such a process is hence known as radiative electron capture. In the non-relativistic regime, REC cross section falls off much slower compared to its non-radiative counterpart, only as v^{-5} [13] for high collision velocities (see figure 1.1(a)).

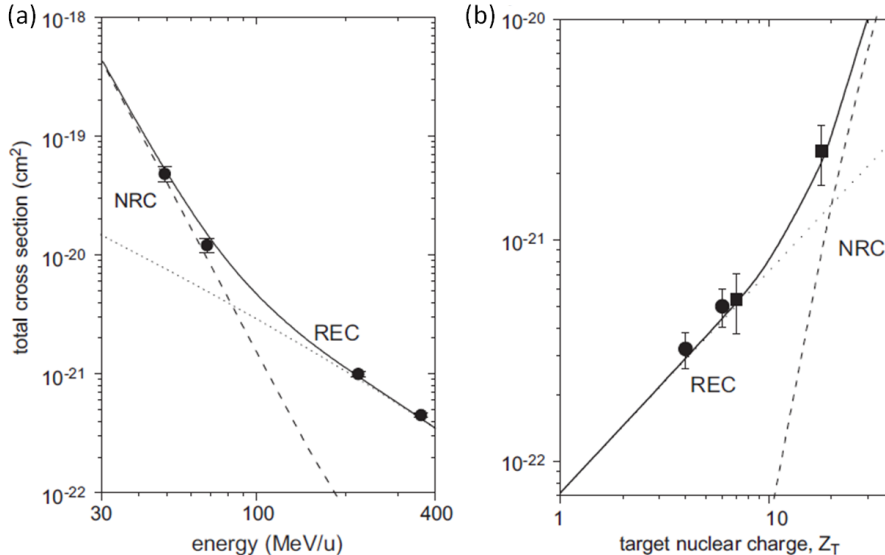


Figure 1.1: (a): Total electron capture cross sections (solid line) for bare uranium ions colliding with a nitrogen target as a function of ion beam energy. The dashed line is the contribution of the non-radiative capture and the dotted line shows that of the REC. (b): Total electron capture cross section for bare uranium ions with 295 MeV/u of kinetic energy as a function of the atomic number of the target Z_T . Figure reproduced from [5].

In asymptotic relativistic regime, though, cross section of both nonradiative and radiative processes scales inversely proportional to the collision energy, E [1]:

$$\sigma_{\text{EC}} \propto E^{-1}. \quad (1.3)$$

For a free electron, capture can not take place at all without the photon emission to conserve the energy and momentum. Therefore, qualitatively speaking, for those loosely bound electrons, either in a low- Z target or in the outer shells, REC would be a preferred, if not the only process for charge exchange in a high energy collision (see figure 1.1(b)). From this point of view, REC mechanism is already worth attention.

Moreover, in high energy collisions, a loosely bound target electron may be considered kinematically free. Thus the REC process may be approximately viewed as the radiative recombination (RR) of a free electron, which in turn, is the time-reverse of the atomic photoelectric effect, one of the most basic form of light matter interaction. Consequently, the measurements of the REC of heavy ions offer a unique opportunity to study strong field effects of the photoionization, especially when the properties of interest are not directly accessible in an ionization experiment [6].

Even more, the electron capture (and other charge exchange) processes are inevitable in almost each step of any kind of experiment concerning highly-charged ions: from the production of ions to the transportation and storage. In order to study other atomic reactions, one usually needs to subtract this omnibackground to deduce the effects of interest.

All in all, the well-refined REC process deserves peculiar attention. However, because of the lack of efficient polarimetric techniques,³ the spectroscopic studies of REC were mainly restricted to the determination of angular distributions and the absolute cross section [6] without resolving the polarization of the emitted photons, until the recent development of segmented hard X-ray detectors enabled precise and efficient Compton polarimetry measurements [14–16].

A study in this direction started in 2006, when the degree of linear polarization of REC into the K-shell of bare ions was measured for the first time using a 4×4 pixel germanium detector [17]. Certain depolarization effects were observed, which was theoretically predicted by Fritz Sauter more than half a century ago [18].

Later detectors with a much finer segmentation (more than 1000 pseudo-pixels) have become available, resulting in a precise determination of the Lyman- α_1 polarization in hydrogen-like uranium [19] and the observation of spin-transfer effects in polarized-electron Bremsstrahlung [20]. There was also a series of measurements aiming for a more precise polarization study of the REC process [21–23], however only a preliminary analysis of the obtained data was performed at that time.

Above listed perspectives and shortcomings motivate the present work. By optimizing and extending the analysis routines originally developed by G. Weber [24], the aim of this work is to form a reliable basis of analyzing algorithms of estimating the linear polarization properties from the data obtained with segmented X-ray detectors, which, as will become clear in the course of this report, is a demanding task.

³For typical projectile energies of the order of 100 MeV/u and capture into high- Z ions, the emitted REC photons have typical energies of the order of 100 keV, for which suitable polarimetric techniques are usually based on Compton scattering (see chapter 2 and references therein for more information).

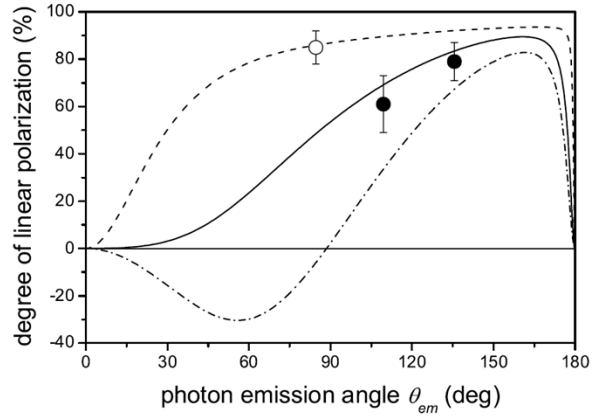


Figure 1.2: Polarization of the uranium K-REC radiation as a function of the photon emission angle in the projectile frame of reference, compared with predictions of a fully relativistic theory. Three collision energies are given: 98 MeV/u, open symbol (for experimental data) and dashed line (for theory); 400 MeV/u, the solid symbols and the full line; 800 MeV/u, dash-dotted line. Figure reproduced from [17].

The thesis is structured as follows: in chapter two, basic notations required for further discussions and an overview of relevant physics processes will be given; chapter three serves to describe the REC process from the theoretical point of view, followed by a presentation of the experimental equipment and techniques in chapter four; in chapter five, the results of this study will be demonstrated; chapter six is devoted to additional experimental studies on radiation yields at high-power lasers that are not directly connected to the REC process, and finally in chapter seven, some conclusion remarks together with outlooks will given.

2 Physics Background

The study of radiative electron capture (REC) is a rather miscellaneous subject, which involves the coupling of the matter and light in a quantum mechanical as well as relativistic way. In this chapter, some basic concepts including basic notations, conventions and the most relevant interaction processes will be briefly reviewed, such that the minimum required knowledge for understanding the following text is covered.

2.1 Basic Concepts

2.1.1 Cross Section

When a beam of particles impinges on a target, some may pass through without any interaction, others may change their directions and energies, and others may even disappear due to interacting with the target (see figure 2.1). The measure for the probability of these interactions to occur is generally given as the cross section, denoted by σ .

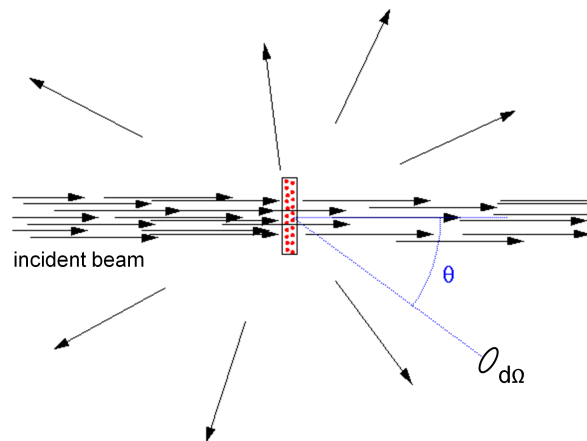


Figure 2.1: Illustration of the cross section as a measure for the likelihood of a certain reaction in case of a scattering process. Each scattering center (red) is associated with a certain geometrical area.

Formally, the differential cross section is defined as the ratio of the number of particles scattered¹ into unit solid angle $d\Omega$ in unit time, N_s , divided by the incident particle flux F :

$$\frac{d\sigma}{d\Omega} = \frac{N_s}{F}. \quad (2.1)$$

For a single quantum mechanical particle, this ratio may be reformulated in terms of the probability current [25]:

$$\frac{d\sigma}{d\Omega} = |f(\theta, \varphi)|^2, \quad (2.2)$$

where $f(\theta, \varphi)$ is the quantum amplitude associated with the interaction, e.g. scattering.

Judging from the dimension of the particle flux, [L^{-2}], or equivalently, from the dimension of the quantum amplitude, [L], the cross section has the dimension of area, which can be heuristically understood as the geometrical cross-sectional area of the target intersecting the beam. However, this picture should not be taken as real measure of physical dimension of the target. For historical reasons, the unit of cross section is usually given in barn (symbol b), with $1 \text{ b} = 10^{-24} \text{ cm}^2$.

The differential cross section is usually a function of energy of the incoming particle and the angle into which the particle is scattered. The integration of the differential cross section over the full solid angle gives the total cross section for a process at given energy E :

$$\sigma(E) = \int \frac{d\sigma(E, \Omega)}{d\Omega} d\Omega. \quad (2.3)$$

For many practical applications, e.g. shielding of high-energy radiation, it is sufficient to know the total cross section of a certain interaction process. However, for some usages such as tracking the propagation of radiation through matter, differential cross sections are necessary because the direction into which outgoing particles are emitted after an interaction (and sometimes also the polarization properties of these particles) might be of relevance. Furthermore, the relative angular distributions, which are sometimes even easier to measure than total cross sections, lend more insight into detailed dynamics of the reactions than the absolute total cross sections.

In the ion-atom collision experiments concerned in this work, the typical energy of the projectile is usually relativistic, therefore it is beneficial to be familiar with the notions of special relativity. The following two subsections will be devoted for this purpose.

¹Here “scattering” refers to interactions of any kind that leads to the outgoing particle emitted into the direction of interest.

2.1.2 Four-vector

Human intuition tells that we are living in a three dimensional space where a scalar-like time constantly flows. However, since the discovery of special theory of relativity, space and time are regarded not severely different any more. Instead, one can treat space and time on a same footing and say that we are living in a “3+1” dimensional spacetime, which mathematicians are used to call Minkowski space. To represent a point in Minkowski space, a vector of four components is necessary, hence such kind of vectors are called four-vectors (or 4-vectors).

A four-vector, x , for spacetime coordinates can be defined in a contravariant manner as x^μ , $\mu = 0, 1, 2, 3$ with an upper index, where $x^0 = ct$, represents the time-like component with t being the time and c the vacuum speed of light; x^i , $i = 1, 2, 3$ are the three space-like coordinates. Here the standard convention states that Greek indices take values for all time and space components whereas Latin indices take values only for spatial components. By multiplying the Minkowski metric tensor $\eta_{\mu\nu} = \text{diag}(1, -1, -1, -1)$, the upper indices can be lowered to give the covariant vector

$$x_\mu = \eta_{\mu\nu} x^\nu = (ct, -\mathbf{x}), \quad (2.4)$$

here repeated indices are summed over, following Einstein summation convention.

The inner product (or Minkowski scalar product as analogy to normal vector scalar product) of two spacetime 4-vectors is defined as

$$\eta_{\mu\nu} x^\mu x^\nu = x^\mu x_\mu = x_\mu x^\mu = \eta^{\mu\nu} x_\mu x_\nu = (ct)^2 - |\mathbf{x}|^2. \quad (2.5)$$

Other dynamical 4-vectors are defined in a similar way as the definition of coordinates, e.g. for energy-momentum 4-vector $p^\mu = (E/c, \mathbf{p})$, the inner product reads

$$p^\mu p_\mu = (E/c)^2 - |\mathbf{p}|^2. \quad (2.6)$$

With the help of the 4-vector notations, the Lorentz transformation can be formulated in a clean form, as will be shortly discussed in the next subsection.

2.1.3 Lorentz Transformation

One basic hypothesis of special relativity is that physics law should be invariant under a Lorentz transformation, which, per definition, is a linear transformation, Λ , linking two

spacetime coordinates

$$x'^{\mu} = \Lambda_{\nu}^{\mu} x^{\nu}, \quad (2.7)$$

such that the Minkowski scalar product is preserved:

$$x'^{\mu} x'_{\mu} = x^{\nu} x_{\nu}. \quad (2.8)$$

The general form of the Lorentz transformation will not be explored further, instead, the discussion will be limited to the transformations in standard configurations for clarity and simplicity. A standard configuration has the following meaning:

Consider two inertial frames with Cartesian spacetime coordinates, (ct, x, y, z) and (ct', x', y', z') , respectively, with the origins of both coordinate systems, O and O' , coincident. Assume that the x -axis and the x' -axis are collinear, while the $y(z)$ -axis is parallel to the $y'(z')$ -axis. Assume further that the primed system has relative to the unprimed one a velocity v along the coincident $x(x')$ -axis.

Given the reduced velocity $\beta = v/c$ and Lorentz factor $\gamma = (1 - \beta^2)^{-1/2}$, the explicit form of Lorentz transformation for spacetime coordinates then reads

$$\begin{bmatrix} ct' \\ x' \\ y' \\ z' \end{bmatrix} = \begin{bmatrix} \gamma & -\beta\gamma & 0 & 0 \\ -\beta\gamma & \gamma & 0 & 0 \\ 0 & 0 & 1 & 0 \\ 0 & 0 & 0 & 1 \end{bmatrix} \begin{bmatrix} ct \\ x \\ y \\ z \end{bmatrix}. \quad (2.9)$$

Other dynamical 4-vectors, transform the same way as the coordinates,

$$Z'^{\mu} = \Lambda_{\nu}^{\mu} Z^{\nu}. \quad (2.10)$$

When considering a radiative process, the transformation formulae of relevant quantities such as photon energy, angle and element of solid angle can be given as:

$$\text{photon energy} \quad \hbar\omega' = \hbar\omega\gamma(1 - \beta \cos \theta) \quad (2.11)$$

$$\text{angle} \quad \cos \theta' = \frac{\beta - \cos \theta}{1 - \beta \cos \theta} \quad (2.12)$$

$$\text{element of solid angle} \quad d\Omega' = \frac{d\Omega}{\gamma^2(1 - \beta \cos \theta)^2}, \quad (2.13)$$

where \hbar is the reduced Planck constant and ω denotes the angular frequency of the photon.

2.1.4 Polarization of Photons

A photon, or “light quantum” as it was firstly proposed, is a gauge boson of electromagnetic interaction in the standard model of particle physics. The concept of photon arises from the quantization of the electromagnetic (EM) field. The quantized EM fields should be understood as operator-valued distributions over space and time:

$$\hat{A}(\mathbf{r}, t) = (\hat{\phi}(\mathbf{r}, t), \hat{\mathbf{A}}(\mathbf{r}, t)), \quad (2.14)$$

where $\hat{\phi}(\mathbf{r}, t)$ represents the scalar potential and $\hat{\mathbf{A}}(\mathbf{r}, t)$ the vector potential.

Due to the gauge symmetry² and transverse nature of the EM field, these four apparent degrees of freedom of $\hat{A}(\mathbf{r}, t)$ represent only two physical degrees of freedom. Taking into account the intrinsic angular momentum (spin) of \hbar possessed by a photon, it is convenient to ascribe these two degrees of freedom to the helicity (projection of spin onto the propagation direction) of the photon and express the polarization state of a photon as

$$|\psi\rangle = a_1 | +1\rangle + a_2 | -1\rangle, \quad (2.15)$$

where basis states $| +1\rangle$ and $| -1\rangle$ can be created by the unit vectors of the right- and left-handed (circular) polarization

$$\begin{aligned} \hat{\mathbf{u}}_{+1} &= \frac{-1}{\sqrt{2}}(\hat{\mathbf{u}}_x + i\hat{\mathbf{u}}_y) \\ \hat{\mathbf{u}}_{-1} &= \frac{1}{\sqrt{2}}(\hat{\mathbf{u}}_x - i\hat{\mathbf{u}}_y), \end{aligned} \quad (2.16)$$

respectively, with the z -direction of the Cartesian coordinate being the propagation direction. Specifically, to create a linearly polarized photon, the unit polarization vector can be parameterized as

$$\hat{\mathbf{u}}(\phi) = \frac{1}{\sqrt{2}}(e^{-i\phi}\hat{\mathbf{u}}_{+1} + e^{i\phi}\hat{\mathbf{u}}_{-1}), \quad (2.17)$$

where ϕ specifies the orientation of the polarization with respect to the above given coordinate system.

A beam of photons, on the other hand, can be described by a state vector as above only if all the photons in the beam are in the same polarization state, which is usually not

²The gauge symmetry prohibits rest mass of the field, therefore a photon should move with a speed of “ c ” in the empty space and there is no rest frame of a photon.

the case. Therefore a compact expression of the polarization properties of the statistical ensemble of photons should be given by a density operator $\hat{\rho}_\gamma$, which, when expressed in the helicity representation, gives a two-by-two matrix with three (real) parameters [26]

$$\langle \mathbf{k}\lambda | \hat{\rho}_\gamma | \mathbf{k}\lambda' \rangle = \frac{1}{2} \begin{bmatrix} 1 + P_3 & -P_1 + iP_2 \\ -P_1 - iP_2 & 1 - P_3 \end{bmatrix}. \quad (2.18)$$

The P 's in the matrix are the Stokes parameters with

$$P_1 = \frac{I_{0^\circ} - I_{90^\circ}}{I} \quad (2.19)$$

$$P_2 = \frac{I_{45^\circ} - I_{135^\circ}}{I} \quad (2.20)$$

describing the degrees of linear polarization with respect to the x - y axes and the diagonal directions, respectively, and

$$P_3 = \frac{I_+ - I_-}{I} \quad (2.21)$$

describing the degree of circular polarization. Here I stands for the total intensity of the photon beam whereas the I 's with subindices represent the intensities that could be transmitted by the corresponding ideal polarization filters.

For experimental studies it is more convenient to combine P_1 and P_2 to represent the total degree of linear polarization of a photon beam in terms of

$$P_L = \sqrt{P_1^2 + P_2^2}. \quad (2.22)$$

The polarization of the beam can also be illustrated by an ellipse as shown in figure 2.2 with the relative length of the principle axes, parameterized by χ , and the orientation of the linear polarization with respect to the given x - y coordinate system, ϕ , defined in terms of the Stokes parameters by the two ratios

$$\tan 2\chi = \frac{P_3}{P_L} \quad \text{and} \quad \tan 2\phi = \frac{P_2}{P_1}. \quad (2.23)$$

There exist two limiting cases for a polarization ellipse: the completely circularly polarized beam ($P_L = 0$, $|P_3| = 1$), which will be illustrated by a circle; and the fully linearly polarized one ($P_L = 1$, $P_3 = 0$), which will be a line. Any intermediate case will give a true ellipse and is therefore also referred to as elliptically polarized light.

To measure the polarization of photons with different energies, there are several po-

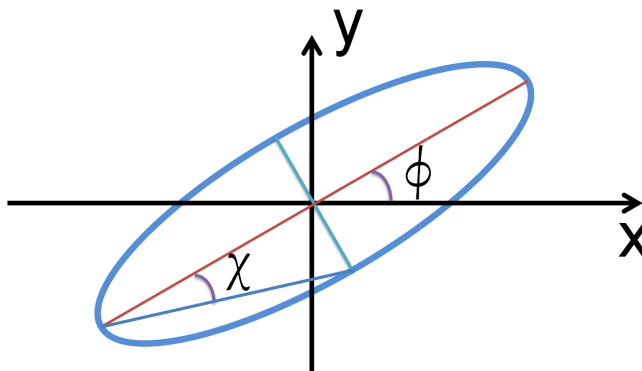


Figure 2.2: The polarization properties of light can be illustrated by the polarization ellipse. The two angles χ and ϕ are defined in equation (2.23).

larimetric techniques [27–34], among which the one based on Compton scattering [32–34] (see subsection 2.2.2) is employed in this work, as will be discussed in detail later in the section 2.3.

2.2 Hard X-ray Interacting with Matter

To measure and understand the properties of the REC photons, which is typically in the hard X-ray regime of the electromagnetic spectrum, it is necessary to have a basic idea of what kinds of interactions and how likely each of them may take place. This is helpful for analyzing the experimental scenario as well as the facts recorded by the detectors.

Photon interacting with matter has a peculiar feature: when passing through matter, the intensity of a photon beam is only attenuated by the elimination of photons from the beam, whereas the energy of each individual photon does not degrade. This is due to the fact that each time a photon interacts, either through absorption or scattering, it will be removed from the beam entirely.

2.2.1 Photon Absorption

When an atom absorbs completely the energy of a photon and one of its bound electrons gets ejected, this absorption process is described as the photoelectric effect. The vacancy generated will then be filled by subsequent Auger processes and/or atomic transitions that give rise to fluorescence radiation. Dictated by energy conservation, the ejected

photoelectron will have a kinetic energy of

$$T_e = \hbar\omega + V,$$

where \hbar is the reduced Planck constant; ω denotes the angular frequency of the absorbed photon and V represents the (negative-valued) binding energy of the electron. Worth mentioning is that photoelectric effect can only take place with the presence of the nucleus, since without a third party carrying away the recoil momentum, an originally free electron is not able to absorb the photon energy without breaking the law of momentum conservation.

Theoretically, rigorous treatment of the photoelectric effect is difficult because of the complexity of the wavefunctions for the atomic electrons. Hence many approximate approaches have been proposed, which will be discussed in detail in the next chapter.

Figure 2.3 plots the experimentally measured photoelectric cross section against the photon energy for Xe [35]. For photon energies above the K-shell (about 35 keV), it is primarily only the K-electrons involved in the ionization process. This can be qualitatively understood since compared with the outer shells, the wavefunction of K-electrons have the most overlap with the nucleus wavefunction, which is beneficial for momentum transfer. Resonance effects can be clearly seen when the photon energy drops to near the binding energy of K-shell electrons, whereas with only a bit further reduction of photon energy, the cross sections plummet since the energy is not sufficient to ionize K-electrons anymore. This point is hence known as the K-edge of the photoionization. Similar behaviour also occur at the L-, M- and other edges.

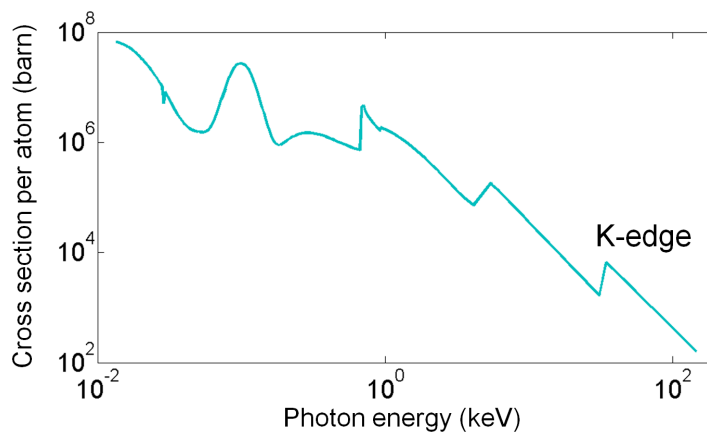


Figure 2.3: Total photoionization cross section for xenon as a function of incident photon energy.[35]

When the photon energy is off-resonance, the cross section of ionization scales roughly according to the following relation [36]:

$$\sigma \propto Z^n \omega^{-7/2}, \quad (2.24)$$

with the exponent n of the atomic number Z varying between 4 and 5 depending on the photon angular frequency ω . There are two consequences of this relation that should be kept in mind: the lower energy a photon has, the more probable it will get absorbed; and high- Z material absorbs photon more effectively. This lends us the instructions when choosing the most efficient detector material for certain photon energy ranges.

Take one of the most common detector material, silicon, as an example, the photon absorption will be the dominate process up to an energy of 50 keV, as can be seen from the figure 2.4 [37]. Above this energy the Compton scattering dominates the interaction, where only a part of the photon energy is detected in an event, as will be shown in the next subsection.

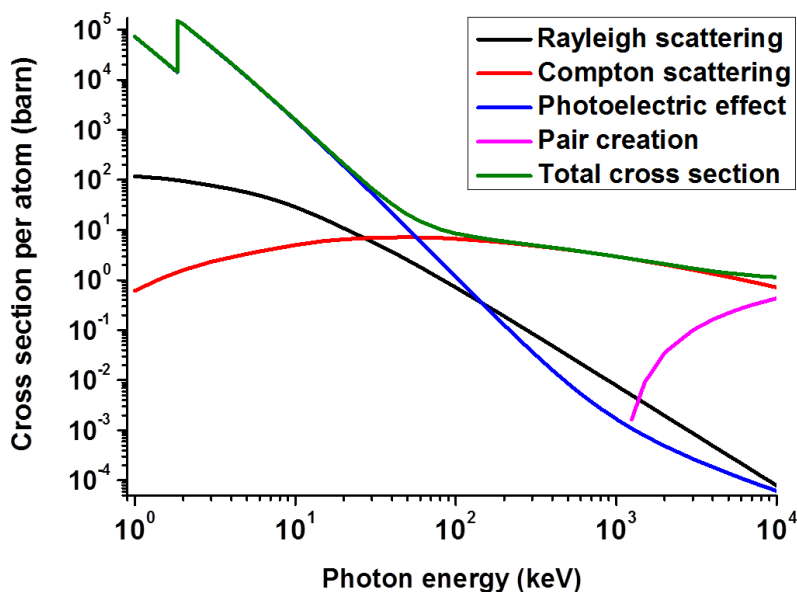


Figure 2.4: Photon interaction cross sections in silicon for the most relevant processes in the hard X-ray regime [37].

2.2.2 Photon Scattering

As the carrier of electromagnetic force, a photon can be scattered by electromagnetic potentials. When the energy of photon does not change before and after the scattering, this process is called elastic, e.g. Rayleigh scattering, where a photon is coherently scattered on the bound electrons of an atom. On the contrary, when the photon energy changes during the scattering, the process is called inelastic, e.g. Compton scattering, where a photon is scattered on a single free electron. In the following discussion, the focus will be put on Compton scattering since it has the most relevance to the scope of this work for two reasons: the energy deposition in the detector and the sensitivity to the incident photon polarization.

Compton Scattering

First observed by Arthur Holly Compton in 1923 [38], Compton scattering gave a convincing verification of the quantum theory of light. Given the electron at rest before scattering, by adopting energy and momentum conservation, one can derive the kinematics of the Compton process (see figure 2.5) as the equation below:

$$\hbar\omega' = \frac{\hbar\omega}{1 + \xi(1 - \cos\theta)}, \quad (2.25)$$

where $\hbar\omega$ and $\hbar\omega'$ are the energies of the incident and the scattered photons, respectively, θ denotes the scattering angle; $\xi = \hbar\omega/m_e c^2$ can be understood as reduced photon energy in the unit of electron rest mass energy.

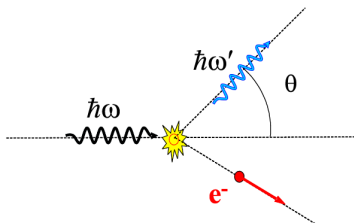


Figure 2.5: Illustration of the process of Compton scattering. A photon scatters on a free electron at rest and transfers a certain amount of energy to the electron.

The kinematics equation (2.25) yields a one-to-one correspondence between scattered photon energy and the scattering angle, which offers the possibility of schematic event selection in the Compton analysis, as will be discussed in the subsection 5.2.2.

The recoil electron gains the kinetic energy given by

$$\Delta E = \hbar\omega - \hbar\omega' = \hbar\omega \frac{\xi(1 - \cos\theta)}{1 + \xi(1 - \cos\theta)}. \quad (2.26)$$

Apparently, the expression above has a maximum when $\theta = \pi$, corresponding to the completely backward scattering of the incident photon. Note that for relative low photon energies ($\xi < 1/2$), the energy of scattered photon is larger than the recoil electron regardless of the scatter angle which may become very beneficial for the Compton analysis discussed in the future chapters, where both the scattering event and the subsequent photoionization event should be identified unambiguously. Whereas for higher incident photon energies ($\xi > 1/2$) this holds true only for the forward directions (relatively small θ), as can be seen in figure 2.6.

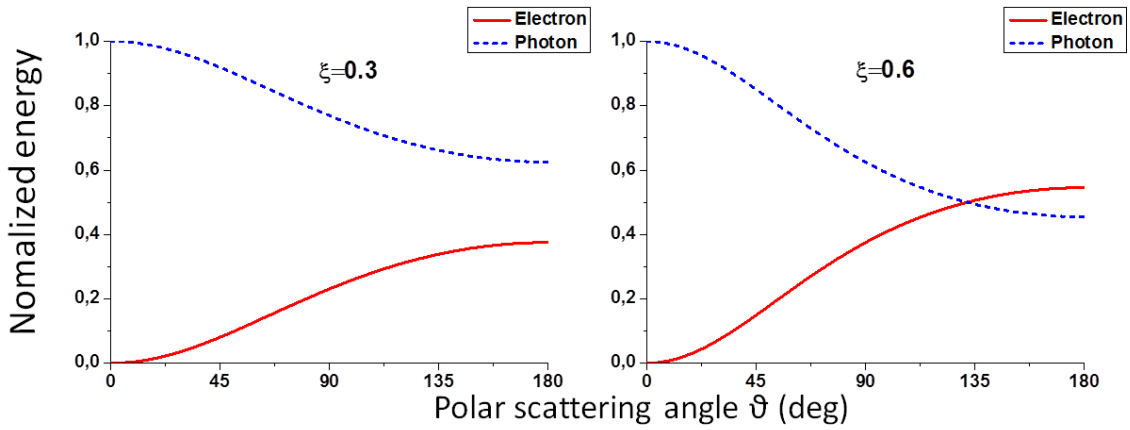


Figure 2.6: Angular dependence of the scattered photon energy and recoil electron energy in unit of the incident photon energy. For $\xi < 0.5$ the scattered photon energy is more than the recoil energy of electron, whereas for values of $\xi > 0.5$ a crossing is observed.

The electrons in the matter are, of course, in most cases bound to the nuclei. However, as long as the energy of photon in question is so high that the binding energy of the electrons are negligibly small, one can safely describe the scatter of a photon on such electrons using Compton scattering formulae (c.f. section 3.1).

Klein-Nishina Formula

The differential cross section of Compton scattering can be given by quantum electrodynamical calculations as [39]

$$\frac{d\sigma}{d\Omega} = \frac{r_e^2 \eta^2}{2} (\eta + \eta^{-1} - 2 \sin^2 \theta \cos^2 \varphi), \quad (2.27)$$

where $r_e = \alpha \lambda_e$ is the classical electron radius with λ_e being the reduced electron Compton wavelength and α fine structure constant; $\eta = (1 + \xi(1 - \cos \theta))^{-1}$ is the ratio of photon energy after and before the scattering; φ is the azimuthal scattering angle, defined as the angle between plane of the incident photon's linear polarization and the plane of Compton scattering (c.f. figure 2.7). This formula was first derived in 1928 by Oskar Klein and Yoshio Nishina, hence known as Klein-Nishina formula.

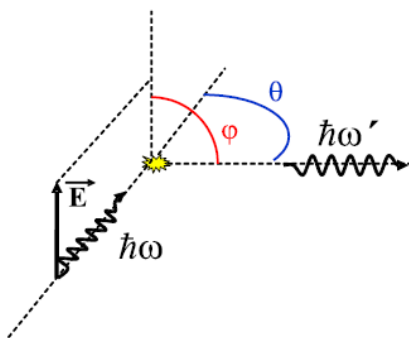


Figure 2.7: Definition of polar scattering angle θ and azimuth angle φ in Compton scattering.

The observation that the differential cross section depends not only on the polar angle but also on the azimuth angle could lend the insight that the Compton scattering process can be employed to study the polarization of the incident photon beam. This subject is known as Compton polarimetry, which will be the topic of next section.

2.3 Compton Polarimetry

The differential cross section described by the Klein-Nishina formula (2.27) indicates that Compton scattering is sensitive to the linear polarization of the incident photon. More specifically, the photon is more likely to be scattered into the direction perpendicular to its polarization than into the parallel one (see figure 2.8). Therefore a linearly polarized photon beam results in an azimuthal modulation of the scattered intensity, which can

be quantified by a modulation fraction defined as

$$M(\varphi) = \frac{I(\varphi_0 + 90^\circ) - I(\varphi_0)}{I(\varphi_0 + 90^\circ) + I(\varphi_0)}, \quad (2.28)$$

where $I(\varphi)$ represent the intensity that could be measured after an ideal linear polarization filter oriented at angle φ with respect to the reaction plane. To achieve the maximal modulation fraction, φ_0 should be chosen along the polarization direction of the incident photon beam. It should be noted that the Compton process itself does not act like a polarization filter on a single-photon level, only the statistical nature of the process allows the observation of the modulation of the scattered intensity.

As shown in the figure 2.8(a), the modulation fraction has higher values for lower energies. For instance, in the case of photon energy below 200 keV the maximum modulation fraction exceeds 90% , and occurs near 90° of the polar scattering angle θ . With increase in energy the peak of the curve shifts slightly to forward angles, which can be taken as an instruction when designing the detector geometry. The modulation fraction drops to zero for small scattering angles and in the case of back scattering. Thus the most useful events are only those scattered into the limited range of angles around $\theta \approx 90^\circ$.

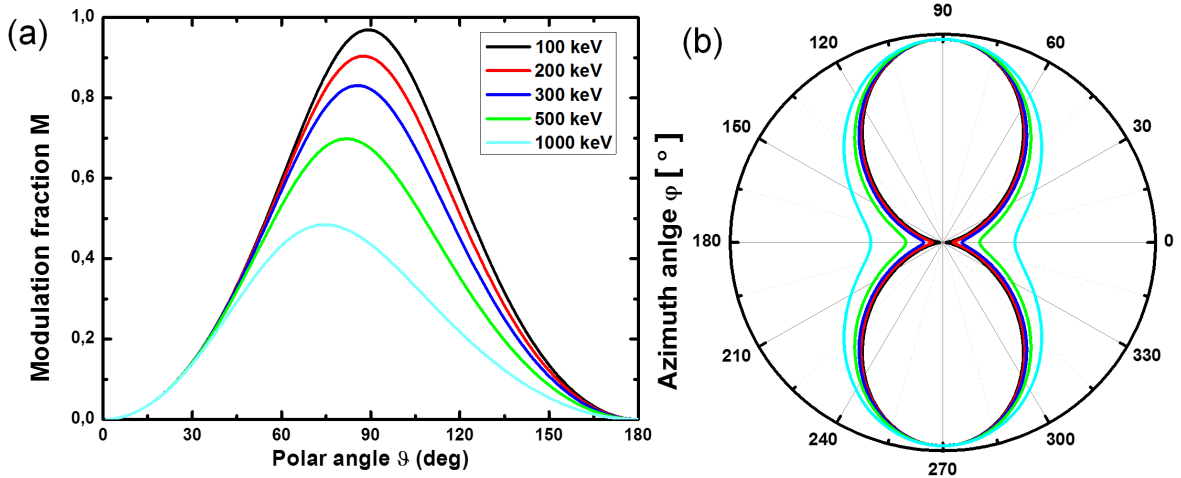


Figure 2.8: (a) Modulation fraction as function of the polar scattering angle θ for various incident photon energies; (b) the corresponding azimuthal distribution at $\theta = 90^\circ$, with $\varphi = 0$ being the polarization direction.

A simple Compton polarimeter consists of a scatterer, and one or more absorbers, situated at $\theta \approx 90^\circ$ with respect to the scatterer (see figure 2.9). Thus the intensities observed by the absorber(s) at different azimuth angles reflect the polarization properties

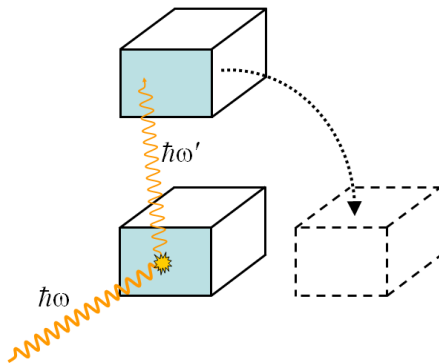


Figure 2.9: A simple Compton polarimeter setup. One detector crystal serves as the scatterer and the other as absorber(s). The azimuthal distribution of the scattered intensity measured by the absorber(s) reflects the polarization property of the incident radiation.

of the incident radiation.

In a real experiment, however, the differential cross section of Compton scattering, $d\sigma/d\Omega$, has to be taken into account as well. To be precise, the parameter to be considered is $M\sqrt{d\sigma/d\Omega}$ because of the square root scaling of statistical uncertainty with respect to the cross section. In order to optimize the polarimeter for this parameter, the absorber(s) should be shifted slightly to the forward direction (see figure 2.10). For practical reasons, though, most currently available Compton polarimeters have their absorber detectors at $\theta \approx 90^\circ$ with respect to the incident X-rays, which, for photon energies below 1 MeV, is also quite near the optimum position.

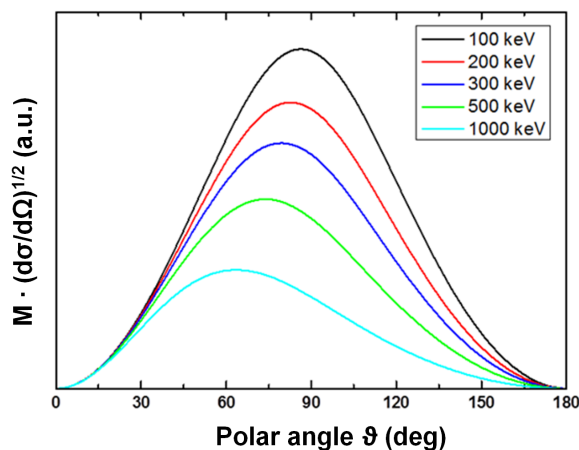


Figure 2.10: Optimization parameter $M\sqrt{d\sigma/d\Omega}$ as a function of the polar angle θ . Optimal absorber position shifts forwards for high photon energies.

Furthermore, because the information about the initial photon polarization will be generally very hard to retrieve after a second scattering, the detector system should be optimized to detect single Compton events, namely, the absorption of the scattered photons should be more likely than a second scattering. A more comprehensive discussion of Compton polarimetry can be found in reference [33].

Since the introduction of highly segmented hard X-ray detectors, the scatterer and absorber of the above mentioned simple Compton polarimeter can actually be a single detector crystal [15, 16]. Such a detector [16] will be introduced in section 4.2.1. Before that the theoretical description of the REC process will be presented in the next chapter.

3 Theoretical Description of REC

Radiative electron capture (REC) is the process where a fast projectile ion captures a bound electron from a target atom with the simultaneous emission of a photon. In a collision of a relativistic highly charged high- Z projectile ion with a low- Z target atom, the REC into a tightly bound state of the projectile, e.g. into K-shell, is almost identical to the time-reverse of the photoionization: the radiative recombination (RR) of a free electron (see figure 3.1)

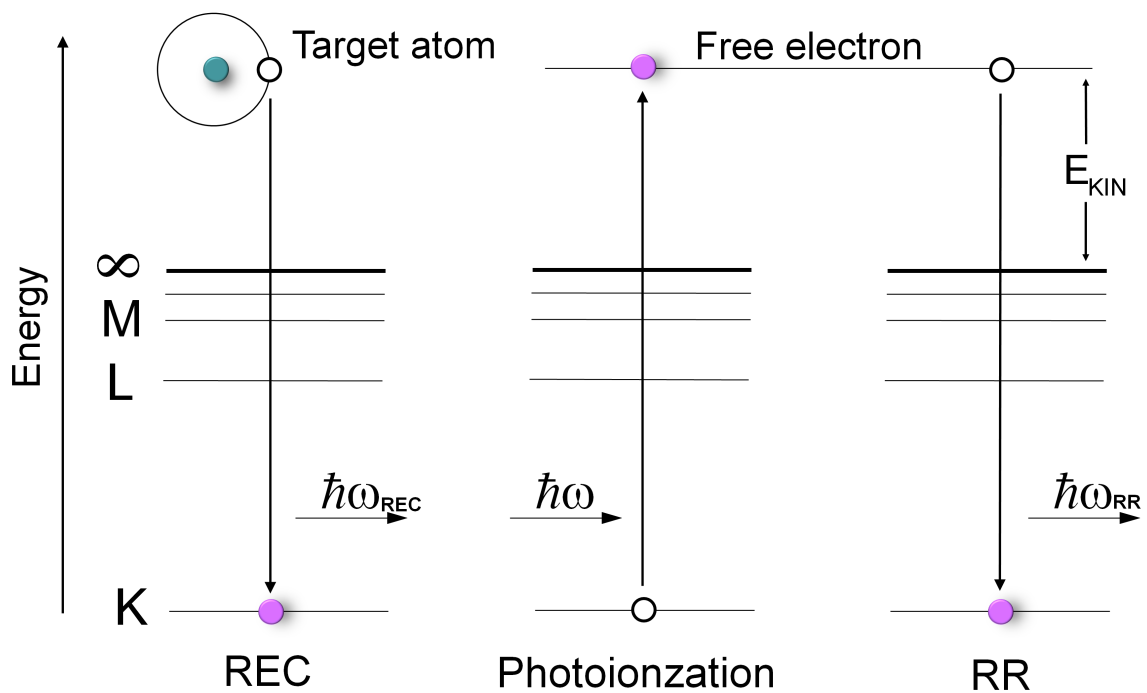


Figure 3.1: Schematic description of the radiative electron capture (REC) as the time-reverse of the photoionization, i.e. radiative recombination (RR).

The theoretical description of the REC process has been formulated in a direct manner using strong-potential Born calculation by Hino and Watanabi [40], where distorted-wave methods was applied to evaluate the transition amplitude. However, this method suffers from spurious contributions when the approximate wavefunctions fail to obey the selection rules followed by REC [41].

Alternatively, there is the method based on impulse approximation (IA), where REC is viewed as modified RR process: The low- Z target is considered as merely providing a momentum distribution and a binding energy to the otherwise free electrons.

In this chapter the IA-based approach [13] will be reviewed for the REC into an initially bare projectile ion, which is also the experimental scenario concerned in this work. With this restriction of the charge state of the projectile, the correlation and shielding effect present in many-electron ions do not come into further discussion.

As a preparation for a fully relativistic description, the conventions adopted are listed below: the two frames of references one naturally encounters in the description of REC, namely, the laboratory frame where the experiments are performed and the moving frame in which the projectile is initially at rest (will be called projectile frame or emitter frame hereafter) where the theories are most conveniently formulated, will be distinguished by a prime attached to each quantity measured in the projectile frame (c.f. subsection 2.1.3). The z -direction of polar coordinate system is chosen as the moving direction of the projectile ion in the laboratory frame, or equivalently, the opposite direction of electron movement when referring to projectile frame. Furthermore, natural units $\hbar = m_e = c = 1$ are used for the tidiness of equations unless explicitly stated otherwise.

3.1 Impulse Approximation

In adopting the impulse approximation (IA), the target is regarded as a collection of independent quasi-free electrons with a momentum distribution determined by the bound electron orbitals of the target. The Coulomb potential of the low- Z target atom will be considered having no further influence on the plane waves representing these quasi-free electrons. Therefore a well-defined asymptotic 4-momentum $q = (\omega_i, q_z, \mathbf{q}_\perp)^T$ can be associated with each target electron having an energy of ω_i , a longitudinal momentum of q_z , and a transverse momentum of \mathbf{q}_\perp .

Then the capture process of this electron can be visualized in the emitter frame as a free electrons moving towards the projectile ion with 4-momentum $q' = \Lambda q$, where Λ

stands for Lorentz transformation, or explicitly

$$q' = \begin{bmatrix} \omega'_i \\ q'_z \\ \mathbf{q}'_{\perp} \end{bmatrix} = \begin{bmatrix} \gamma(\omega_i - vq_z) \\ \gamma(q_z - v\omega_i) \\ \mathbf{q}_{\perp} \end{bmatrix}, \quad (3.1)$$

where $\gamma = (1 - v^2)^{-1/2}$ is the Lorentz factor and v stands for the projectile velocity.

For a high energy collision between a heavy bare ion and a low- Z target atom, the velocity of the captured electron in the projectile frame, \mathbf{v}'_e , is essentially determined by the velocity of the target atom with respect to the projectile, $-\mathbf{v}$. However, the electron bound to the target has a momentum distribution $\rho(q)$, so that there is a momentum spread around the central momentum $\mathbf{q}'_c = -\gamma\mathbf{v}$.

By assuming $q_z \ll \gamma v$, the doubly differential (in photon energy ω' and solid angle Ω') REC cross section can be given by the convolution of the RR cross section and the target electron momentum distribution:

$$\left. \frac{d^2\sigma_{\text{REC}}}{d\omega'd\Omega'} \right|_{\omega'=\omega'_p} = \int d^3q \frac{d\sigma_{\text{RR}}(q')}{d\Omega'} \rho(q) \delta(\omega'_p + \omega'_f - \omega'_i), \quad (3.2)$$

where ω'_p is the energy of the photon to be emitted and ω'_f is the electron energy in the final atomic state. Hence the delta distribution represents the constraint for the energy conservation. It should be noted that the dependence of the RR cross section on the projectile atomic number Z_P and the final state are omitted for brevity.

The above mentioned target momentum distribution can be obtained as the absolute square of the initial electronic wavefunctions in the momentum representation:

$$\rho(q) = |\tilde{\varphi}_i(\mathbf{q})|^2. \quad (3.3)$$

In practice, $\tilde{\varphi}_i(\mathbf{q})$ can be calculated as the Fourier transform of, for example, the Roothaan-Hartree-Fock (RHF) wavefunctions [42].

A qualitative understanding can already be given by a simplified case, i.e. the spherically averaged distribution for a nonrelativistic hydrogen-like system [1]

$$\begin{aligned} \rho(q) &= \frac{1}{n^2} \sum_{lm} |\tilde{\varphi}_{nlm}(\mathbf{q})|^2 \\ &= \frac{8Q_n^5}{\pi^2(|\mathbf{q}|^2 + Q_n^2)^4}, \end{aligned} \quad (3.4)$$

where $\tilde{\varphi}_{nlm}(\mathbf{q})$ is the Fourier transform of the electron wave function for the state characterized by the nonrelativistic quantum numbers $\{n, l, m\}$ and

$$\mathcal{Q}_n = \frac{\alpha Z_T}{n}, \quad (3.5)$$

with α being the fine structure constant, Z_T being the target atomic number, and n the primary quantum number of the target electron in question.

The momentum distribution (3.4) has a maximum at $|\mathbf{q}| = 0$ and a width determined by \mathcal{Q}_n : the distribution gets more concentrate with decreasing of Z_T and increasing of n (c.f. figure 3.2). This quite general feature leads to a simplification of the convolution formula (3.2) when the slow variation of the RR cross section is taken into account. By taking the slow varying RR cross section out of the integral, substituting for the momentum distribution the expression (3.3), and inserting expression (3.1) for initial state energy, one can obtain:

$$\begin{aligned} \left. \frac{d^2\sigma_{\text{REC}}}{d\omega'd\Omega'} \right|_{\omega'=\omega'_p} &= \frac{d\sigma_{\text{RR}}(q')}{d\Omega'} \int d^2q_{\perp} \int dq_z |\tilde{\varphi}_i(\mathbf{q})|^2 \delta(\omega'_p + \omega'_f - \gamma\omega_i + \gamma v q_z) \\ &= \frac{1}{\gamma v} \frac{d\sigma_{\text{RR}}(q'_z)}{d\Omega'} \mathcal{J}(q_z), \end{aligned} \quad (3.6)$$

where

$$\mathcal{J}(q_z) = \int d^2q_{\perp} |\tilde{\varphi}_i(\mathbf{q})|^2 \quad (3.7)$$

is the so-called Compton profile of the target atom, which can be found as tabulated values [43]. The longitudinal component of momentum, q_z , is determined by the integration of the delta distribution as:

$$q_z = -\frac{\omega'_p + \omega'_f - \gamma\omega_i}{\gamma v}, \quad (3.8)$$

whereas its Lorentz transformed counterpart, q'_z , is given by equation (3.1).

So far the effects of the transverse momentum \mathbf{q}_{\perp} , which results in a tilt of the total momentum off the z -axis, have not been considered. This tilt introduces an individual symmetry axis of photon angular distribution for each value of the transverse momentum, therefore, these small deviations have to be integrated over. However, the estimate of the tilt angle [13], $\mathcal{Q}_1/\gamma v$, amounts only about 0.7° with respect to the z -axis for the rather moderate experimental condition considered in this work (150.5 MeV/u Xe⁵⁴⁺ colliding with hydrogen), for higher energies the tilt angle and hence its influence will be even

less. Consequently, it is appropriate [5] to neglect the transverse electron momentum in the IA for practical reasons.

Therefore the expression (3.6) represents the final form of the IA, which is implemented in the code of the REC calculator developed within the framework of this master thesis (see section 5.1). Some spectra produced by this calculator are shown in figure 3.2, where the shape of REC spectra can be described as the Doppler broadened (due to the target Compton profile) RR spectra with the Doppler width characterized by \mathcal{Q}_n as defined in equation (3.5). The peaks are around $q_z = 0$, or equivalently $\omega'_c = \gamma\omega_i - \omega'_f$ with a tendency to shift towards the lower energy direction due to the decreasing RR cross sections for higher energies (c.f. subsection 3.2.3).

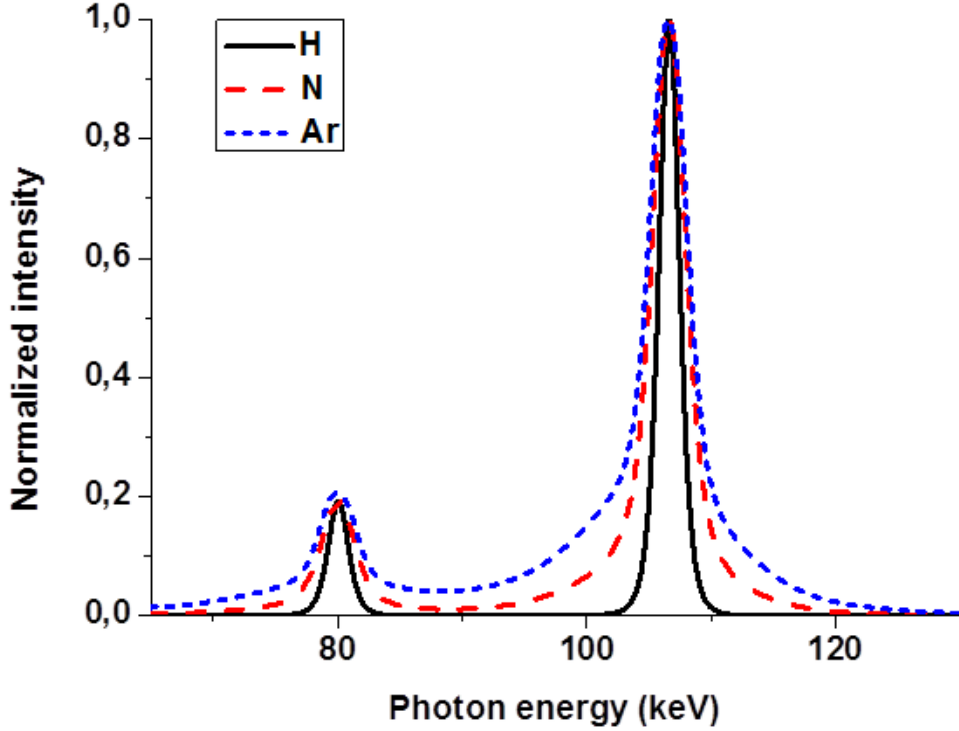


Figure 3.2: REC cross section into K- and L-shell of bare Xe for a H, N, and Ar target at collision energy of 150.5 MeV/u, observed at 90° in the laboratory frame, calculated with the REC calculator developed within this work. The maximum intensity is normalized to 1 for each target species.

At this point, the validity of the above mentioned IA is a critical question to address. Because all the following discussions are based on a valid IA, the next subsection will be devoted to justify this approximation.

3.1.1 Validity of Impulse Approximation

Qualitatively, the IA is expected valid when the energy transferred to the electron in the capture process is much larger than the binding energy of the initial states involved, which seems justified by the experimental conditions: capture into inner shells of a relativistic high- Z projectile from a low- Z target.

To formulate a quantitative criterion for validity, however, the close analogy of REC to Compton scattering from bound electrons can be used, because the IA was successfully applied there to describe the photon scattering (see [44] for more information). In the IA described in [44] a high-energy photon is scattered inelastically by an initially bound electron, leading to the ejection of the recoil electron which is then described by a plane wave. This description has a clear relation to the REC with the projectile ion replacing the photon and the initial electron described by a plane wave.

Due to this close analogy, the criterion for REC [5] can be formulated similarly as equation (5) of reference [44]:

$$\rho_{\text{REC}} = \frac{\alpha Z_T}{nv} \ll 1. \quad (3.9)$$

Using the nonrelativistic relation between projectile energy T_P and its velocity v , the criterion can be expressed in simple term of the experimental parameter T_P as

$$\rho_{\text{REC}} \approx 0.16 \frac{Z_T}{n} (T_P [\text{MeV/u}])^{-1/2} \ll 1, \quad (3.10)$$

which should be satisfied even better for relativistic conditions.

For the experimental condition of this work: $Z_T = 1$, $n = 1$, and $T_P = 150.5 \text{ MeV/u}$, the criterion is well satisfied with $\rho_{\text{REC}} = 0.013 \ll 1$.

Quite generally, because all target electrons will contribute to REC, one has to average over them for a multi-electron target. In that case the large number of slow valence electrons will dominate the few fast inner-shell electrons. In short, the criterion should be well satisfied by realistic experimental conditions.

It should be noted that the quantitative criterion discussed above does not refer to the relation between atomic numbers of the collision system, however, in order to justify the assumption that the target electrons are subject exclusively to the Coulomb field of the projectile¹, the requirement $Z_T \ll Z_P$ must be fulfilled.

¹As a consequence, the initial state can be described by a plane wave and the final state by a bound state of the projectile.

With the IA at hand, the remaining problem is to calculate the properties of RR, which will be the topic of the following two sections, including the approximate approaches in section 3.2, and finally a rigorous method based on density matrix theory to calculate RR cross sections as well as polarization properties in section 3.3.

3.2 Radiative Recombination I: Approximate Methods

As already pointed out, RR is the time-reverse of the photoelectric effect. Therefore the cross section of RR can be obtained from the cross sections of the photoelectric effect by adopting the principle of detailed balance [5, 45]

$$\frac{d^2\sigma_{\text{RR}}}{d\omega'\Omega'} = \frac{\omega'^2}{q'^2} \frac{d^2\sigma_{\text{ph}}}{d\omega d\Omega}. \quad (3.11)$$

For this reason, this section will primarily discuss the photoelectric effect, particularly the approximate treatments. The obtained cross sections will then be converted to RR cross sections using detailed balance.

It will be shown that the angular differential cross sections of RR are dominated by large cancellation effects between retardation and relativistic transformation hence show up in a particular clean manner in the laboratory frame.

3.2.1 Photoelectric Effect

The differential cross section of for a photon with wave vector \mathbf{k} ($|\mathbf{k}| = \omega/c$ with c being the speed of light and ω the angular frequency of the photon) to liberate a bound electron into a continuum state can be given in general as [46]

$$\frac{d\sigma_{\text{ph}}}{d\Omega} \propto |M_{fi}|^2. \quad (3.12)$$

Here the “prime” convention will be temporarily omitted because all quantities are given in emitter frame. The transition matrix element $M_{fi} = \langle \psi_f | \hat{R} | \psi_i \rangle$ can be evaluated in the coordinate representation, $\langle \mathbf{r} |$, as

$$M_{fi} = \int d^3r \psi_f^\dagger(\mathbf{r}) \boldsymbol{\alpha} \cdot \hat{\mathbf{u}} e^{i\mathbf{k}\cdot\mathbf{r}} \psi_i(\mathbf{r}), \quad (3.13)$$

where $\boldsymbol{\alpha}$ is the vector form of Dirac matrices; the unit vector $\hat{\mathbf{u}}$ denotes the polarization of the incident photon; $\psi_f^\dagger(\mathbf{r})$ represents the Hermitian adjoint of the final state spinor

and $\psi_i(\mathbf{r})$ the initial state spinor; the plane wave part $e^{i\mathbf{k}\cdot\mathbf{r}}$ represents the inclusion of all multipole orders, or so called retardation effect.

3.2.2 Born Approximation

The simplest case to consider is the ionization of a nonrelativistic K-shell electron. Given the incident photon has much more energy than needed to liberate the K-shell electron, the final state electron with momentum \mathbf{q} can be described by a plane wave

$$\psi_f(\mathbf{r}) = e^{i\mathbf{q}\cdot\mathbf{r}}. \quad (3.14)$$

The Dirac matrices $\boldsymbol{\alpha}$ then reduce to a nonrelativistic current operator $\hat{\mathbf{p}} = -i\nabla$ [25], which can act to the left on the $\exp(i\mathbf{q}\cdot\mathbf{r})$ term to give

$$M_{fi} \propto \mathbf{q} \cdot \hat{\mathbf{u}} \int d^3r e^{i(\mathbf{k}-\mathbf{q})\cdot\mathbf{r}} \psi_i(\mathbf{r}), \quad (3.15)$$

which is proportional to the Fourier transform of the initial wave function.

The dot product in the equation above can be evaluated in spherical coordinates as

$$\mathbf{q} \cdot \hat{\mathbf{u}} = q \sin \theta \cos \varphi \quad (3.16)$$

with θ being the polar angle (with respect to the momentum of incident photon), and φ denoting the azimuth angle (with respect to the photon polarization).

On insertion of the hydrogen-like K-shell electron wave function for the initial state

$$\psi_i(\mathbf{r}) = \sqrt{\frac{Z^3}{\pi a_0^3}} e^{-\frac{Zr}{a_0}}, \quad (3.17)$$

with Z as the atomic number and $a_0 = \hbar^2/m_e e^2$ the Bohr radius, equation (3.15) yields

$$\frac{d\sigma_{\text{ph}}}{d\Omega} \propto \frac{\sin^2 \theta \cos^2 \varphi}{(1 - v \cos \theta)^4} Z^5, \quad (3.18)$$

where v stand for the velocity of the ejected electron. For unpolarized photons, the $\cos^2 \varphi$ term should be replaced by 1/2.

The observation that most of the electrons are emitted in the direction $\hat{\mathbf{u}}$ ($\theta = 90^\circ$) and no electrons are emitted in the direction of \mathbf{k} ($\theta = 0^\circ$) can be intuitively understood from a classical picture of electromagnetic waves. A quantum interpretation is that the

nonrelativistic absence of electron spin forbids forward or backward emission, since the electron cannot carry away the photon spin of unity, as shown in figure 3.3.

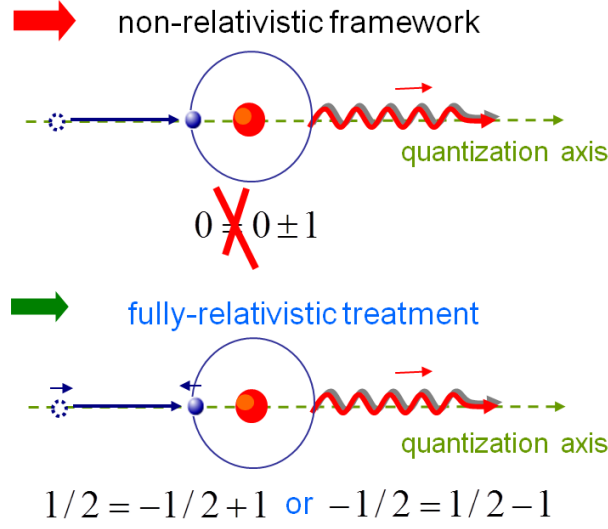


Figure 3.3: Comparison between non-relativistic description and a fully relativistic one. In the former case, the electron spin does not couple to the orbital angular momentum therefore the forward (backward) emission of photon is forbidden due to angular momentum conservation. Whereas in the latter, the angular momentum can be conserved by the flip of the spin projection, therefore forward (backward) emission is allowed.

If one adopts further dipole approximation, i.e. $\exp(i\mathbf{k} \cdot \mathbf{r}) \rightarrow 1$, no angular dependence appears in the denominator and the differential cross section of photoelectric effect is given by a pure $\sin^2 \theta$ distribution in the emitter frame.

From now on, the “prime” convention is recovered to continue the discussion of RR. The detailed balance preserves the proportionality, as a consequence the differential cross section for radiative recombination is given by:

$$\frac{d\sigma_{\text{RR}}}{d\Omega'} \propto \frac{\sin^2 \theta'}{(1 - v \cos \theta')^4}. \quad (3.19)$$

By transforming this expression into laboratory frame with help of formulae for angle and solid angle element as in equations (2.12) and (2.13)

$$\cos \theta' = \frac{v - \cos \theta}{1 - v \cos \theta}$$

$$\frac{d\Omega'}{d\Omega} = \frac{1}{\gamma^2 (1 - v \cos \theta)^2},$$

the final result reads

$$\frac{d\sigma_{\text{RR}}}{d\Omega} \propto \sin^2 \theta, \quad (3.20)$$

which is a pure $\sin^2 \theta$ distribution in the laboratory frame.

This peculiar cancellation between the effects of the retardation, i.e. of higher multipoles (leading to a deviation from a $\sin^2 \theta$ distribution in equation (3.18)) and the Lorentz transformation to the laboratory system has been first observed by Spindler et al. [47]. It will be shown by the rigorous calculations in a later section that this general behavior is still approximately valid for rather high projectile energies.

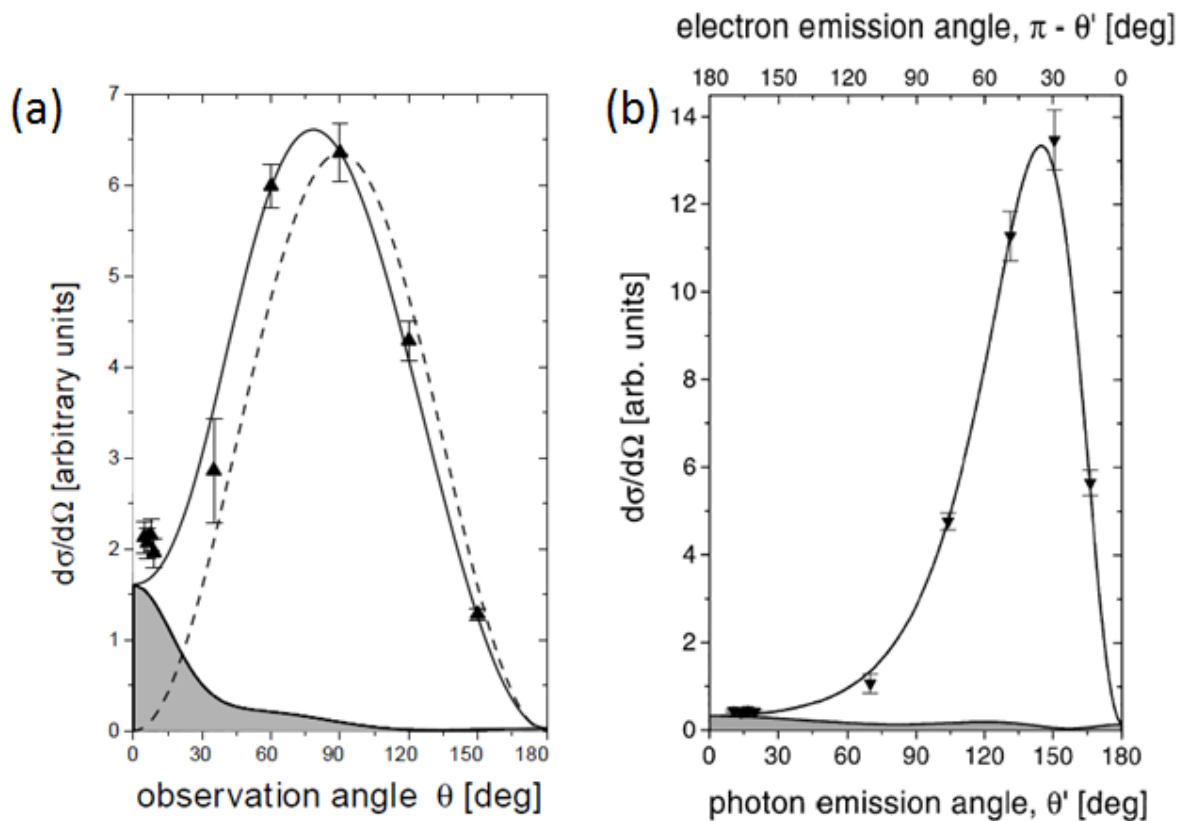


Figure 3.4: (a) Experimental angular distribution for REC into the K-shell of bare uranium in collisions with N_2 at a kinetic energy of 309.7 MeV/u compared to the fully relativistic theoretical prediction. The latter was scaled to coincide with the experimental value at 90° (laboratory system). The finite cross section near zero degree is almost exclusively due to the so-called spin-flip contribution, while the dashed line illustrates the non-relativistic $\sin^2 \theta$ emission pattern. (b) Same as figure (a) but plotted in the emitter frame which corresponds to the electron emission characteristics for the photoionization process. Here the spin-flip contribution is smeared out and hardly detectable. Figure reproduced from Th. Stölker et al. [6].

The cancellation effect of the RR/REC angular distribution yields a significant advantage of REC experiments over the direct photoionization experiments, namely, the clear identification of the magnetic spin-flip transitions leading to a non-zero emission probability along the collision axis (c.f. figure 3.3). This is illustrated in figure 3.4, where the spin-flip contribution to REC photons' angular distribution is detectable but to the photoelectrons' distribution (practically) not, because the Lorentz transformations of angle and solid angle smear the contribution over the whole angular range in the latter case.

3.2.3 Stobbe Formula

The Born approximation described in the previous subsection is inadequate for larger values of Z or if the photon energy is not large enough, in which case the ejected electron is strongly affected by the Coulomb potential of the mother nucleus and therefore has to be described by Coulomb-continuum wavefunctions instead of a simple plane wave. Following this consideration, Stobbe [48] has derived the photoelectric cross section per K-shell electron within dipole approximation. By applying detailed balance, the Stobbe formula gives the RR cross section for recombination into an empty K-shell:

$$\sigma_{\text{RR}}^{\text{Stobbe}} = \frac{2^8 \pi^2}{3} \lambda_c^2 \left(\frac{\nu^3}{1 + \nu^2} \right)^2 \frac{e^{-4\nu \cot^{-1} \nu}}{1 - e^{-2\pi\nu}} \quad (3.21)$$

where $\lambda_c = \hbar/m_e c$ is the (reduced) Compton wavelength of the electron and $\nu = \alpha Z/\beta$ is the Sommerfeld parameter. The constants in front of the ν -dependent terms make up a factor of 9164.7 barn. For the experimental parameters (150.5 MeV/u Xe⁵⁴⁺ colliding with H), the ν -dependent part amounts 5×10^{-3} , and therefore the total RR cross section per K-shell vacancy per target electron is roughly 46.25 barn.

The Stobbe formula proves to be quite useful to estimate the total cross section of the REC into the K-shell up to projectile energies of the order of 1 GeV/u, corresponding to electron kinetic energies below the electron rest energy, as shown by figure 3.5. However, its pure dipole characteristics ($\sin^2 \theta$ distribution and 100% polarization) is not able to describe the subtle details of the angular distribution of of RR/REC photons, such as the contribution from spin-flip transitions (c.f. figure 3.4 and reference [6]) and the depolarization caused by the magnetic field, as will be shown by the exact calculations discussed in the next section.

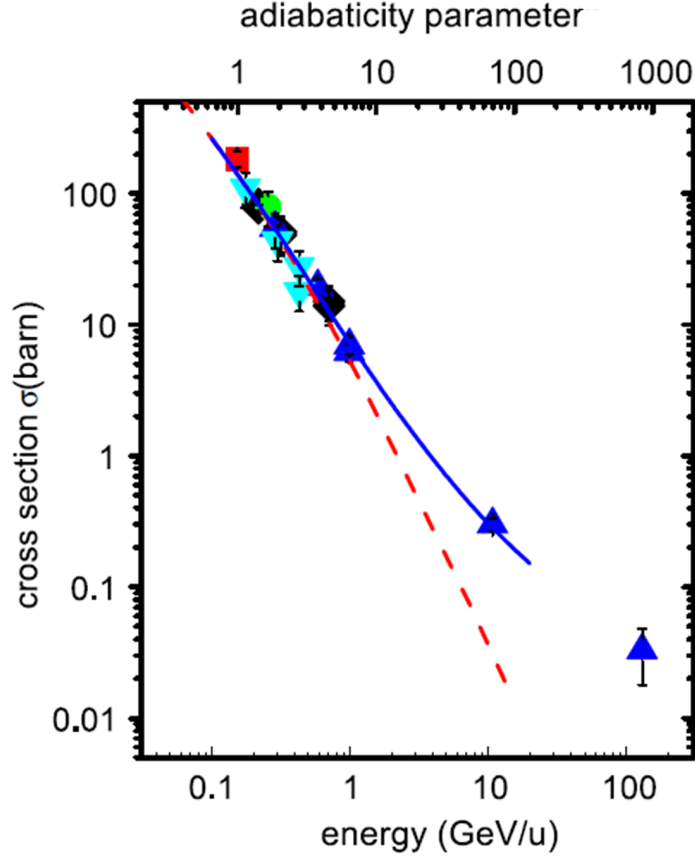


Figure 3.5: Total electron capture cross section per target electron for heavy bare ions ($Z_P \geq 54$) in collision with light target. The blue line shows the fully relativistic calculation and the red dashed line is the prediction of the non-relativistic dipole approximation, which is in good agreement with the experimental finding up to an energy of the order of GeV/u [5].

3.3 Radiative Recombination II: Density Matrix Theory

Following closely the approach of A. Surzhykov et al. [49, 50], the density matrix formalism is applied in this section to calculate the cross section as well as the photon polarization of the RR process in a fully relativistic manner. It should be pointed out that the nucleus will be treated as a spinless point with infinite mass whereas the QED effects such as vacuum polarization and electron self energy will not be included neither.

Thus the initial state is an electron with an asymptotic 4-momentum p and spin projection m_s , which can be represented by a density operator $\hat{\rho}_e$.

Using the transition operator $\hat{R}(\mathbf{k}) = \boldsymbol{\alpha} \cdot \hat{\mathbf{u}} \exp(i\mathbf{k}\mathbf{r})$ as described in preceding subsec-

tion 3.2.1. The final state density operator can be expressed as

$$\hat{\rho}_f = \hat{R}^\dagger \hat{\rho}_e \hat{R}, \quad (3.22)$$

which describes the emitted photon with wave vector \mathbf{k} and helicity λ (projection of spin onto the direction of \mathbf{k}) plus the electron in a bound state $|J_b \mu_b\rangle$.

To measure the angular distribution of the emitted photons without resolving the polarization of the light, the spin state of the bound electron, and the spin projection of the initial electron, a projector of the following form

$$\hat{P}_k = \sum_{m_s \lambda \mu_b} |p m_s\rangle |\mathbf{k} \lambda\rangle |J_b \mu_b\rangle \langle J_b \mu_b| \langle \mathbf{k} \lambda| \langle p m_s| \quad (3.23)$$

can be taken to project out all those quantum states of the final system that results in a count in the detector systems, which leads to an angular distribution as in [13]

$$\text{Tr}(\hat{P}_k \hat{\rho}_f) = \frac{1}{2} \sum_{m_s \lambda \mu_b} \left| \langle J_b \mu_b, \mathbf{k} \lambda | \hat{R}^\dagger |p m_s\rangle \right|^2. \quad (3.24)$$

To retrieve the photon polarization, a set of projectors can be formed similarly. However, there is a more convenient way: to retain the reduced density operator of the outgoing photons, $\hat{\rho}_\gamma = \text{Tr}_{\mu_b}(\hat{\rho}_f)$. Since, as already discussed in the subsection 2.1.4 of the physics background, the photon density matrix

$$\langle \mathbf{k} \lambda | \hat{\rho}_\gamma | \mathbf{k} \lambda' \rangle = \frac{1}{2} \begin{bmatrix} 1 + P_3 & -P_1 + iP_2 \\ -P_1 - iP_2 & 1 - P_3 \end{bmatrix} \quad (3.25)$$

is directly related to the Stokes parameters P_1, P_2 , and P_3 of the emitted light, which are also used experimentally as measure of the polarization properties.

The photon matrix elements

$$\langle \mathbf{k} \lambda | \hat{\rho}_\gamma | \mathbf{k} \lambda' \rangle = \sum_{\mu_b m_s m'_s} \langle p m_s | \hat{\rho}_e | p m'_s \rangle \langle J_b \mu_b, \mathbf{k} \lambda | \hat{R}^\dagger | p m_s \rangle \langle p m'_s | \hat{R} | J_b \mu'_b, \mathbf{k} \lambda' \rangle \quad (3.26)$$

are essentially determined by the transition matrix elements known from the previous discussion

$$\langle J_b \mu_b, \mathbf{k} \lambda | \hat{R}^\dagger | p m_s \rangle = \int d^3r \psi_{J_b \mu_b}^\dagger(\mathbf{r}) \boldsymbol{\alpha}^\dagger \cdot \hat{\mathbf{u}}_\lambda^* e^{-i\mathbf{k}\cdot\mathbf{r}} \psi_{p m_s}(\mathbf{r}), \quad (3.27)$$

which present the general form of the relativistic photon-electron interaction in a one-electron ion. For its evaluation, the quantization axis of spin is usually chosen either as the photon direction, which results in generally faster numerical calculations [13, 49], or as the electron momentum, which allows for the inclusion of definite spin states of the incident electron or the residual ion and therefore an appropriate interpretation of spin-flip, at the cost of more computation time. For the approach discussed in this section, the latter is adopted.

Once the quantization axis is fixed as the electron momentum direction, the photon field needs to be rotated to this direction, which can be achieved by Wigner rotation of its multipole expansion:

$$\hat{\mathbf{u}}_\lambda e^{i\mathbf{k}\cdot\mathbf{r}} = \sqrt{2\pi} \sum_{L=1}^{\infty} \sum_{M=-L}^{M=L} i^L \sqrt{2L+1} \mathcal{A}_{LM}^\lambda D_{M\lambda}^L(\mathbf{k} \rightarrow \mathbf{z}), \quad (3.28)$$

where the summation runs over all azimuthal quantum number L and magnetic quantum number M ; $D_{M\lambda}^L(\mathbf{k} \rightarrow \mathbf{z})$ denotes the Wigner rotation and the multipole component \mathcal{A}_{LM}^λ can be decomposed further into the magnetic and electric parts as

$$\mathcal{A}_{LM}^\lambda = \mathcal{A}_{LM}(m) + i\lambda \mathcal{A}_{LM}(e). \quad (3.29)$$

By expanding the product of two Wigner rotations, the photon density matrix 3.26 can be represented as

$$\langle \mathbf{k} \lambda | \hat{\rho}_\gamma | \mathbf{k} \lambda' \rangle = \sum_{\nu \mu} D_{0\mu}^\nu(0, \theta, 0) \sum_{L \pi L' \pi'} \beta_{L \pi L' \pi'}^{\nu \mu}(\lambda, \lambda'), \quad (3.30)$$

where θ denotes the angle between photon emission and electron momentum. The angular parameter

$$\begin{aligned} \beta_{L \pi L' \pi'}^{\nu \mu}(\lambda, \lambda') &= \sum_{m_s \mu_b} i^{L'+\pi'-L-\pi} (-1)^{m_s-\mu_b} \sqrt{(2L+1)(2L'+1)} \langle p m_s | \hat{\rho}_e | p m_s \rangle \\ &\quad \times \lambda^\pi \lambda'^{\pi'} \langle L' m_s - \mu_b L \mu_b - m_s | \nu 0 \rangle \langle L \lambda' L - \lambda | \nu \mu \rangle \\ &\quad \times \langle p m_s | \boldsymbol{\alpha} \mathcal{A}_{L m_s - \mu_b}^\pi | \kappa_b \mu_b \rangle^* \langle p m_s | \boldsymbol{\alpha} \mathcal{A}_{L' m_s - \mu_b}^{\pi'} | \kappa_b \mu_b \rangle \end{aligned} \quad (3.31)$$

represents the contribution of each multipole order of the radiation field. The $\langle \dots | \dots \rangle$'s are Clebsch-Gordan coefficients and $\langle p m_s | \boldsymbol{\alpha} \mathcal{A}_{LM}^\pi | \kappa_b \mu_b \rangle$ denotes the matrix element for either the electric ($\pi = 1$) or magnetic ($\pi = 0$) multipole free-bound transition of the

electron.

A further simplification can be achieved by decomposing the free electron wave function $|p m_s\rangle$ into a partial wave expansion

$$|p m_s\rangle = \sum_{\kappa} i^l e^{i\Delta_{\kappa}} \sqrt{4\pi(2l+1)} \langle l 0 \frac{1}{2} m_s | j m_s \rangle |E \kappa j m_s\rangle, \quad (3.32)$$

where the summation runs over all partial waves $|E \kappa j m_s\rangle$ with the energy of E and the Dirac angular momentum quantum number $\kappa = \pm(j + 1/2)$; the quantum number $l = j \pm 1/2$ for the nonrelativistic orbital angular momentum represents the parity of the partial wave whereas the Δ_{κ} is the Coulomb phase shift.

Making use of the Wigner-Eckart theorem, the problem reduces to the evaluation of the reduced density matrix elements $\langle E \kappa j || \alpha \mathcal{A}_L^{\pi} || n_b j_b \rangle$ describing the interaction of an electron with the radiation field for a standard free-bound transition, which can be calculated with procedure introduced in [51].

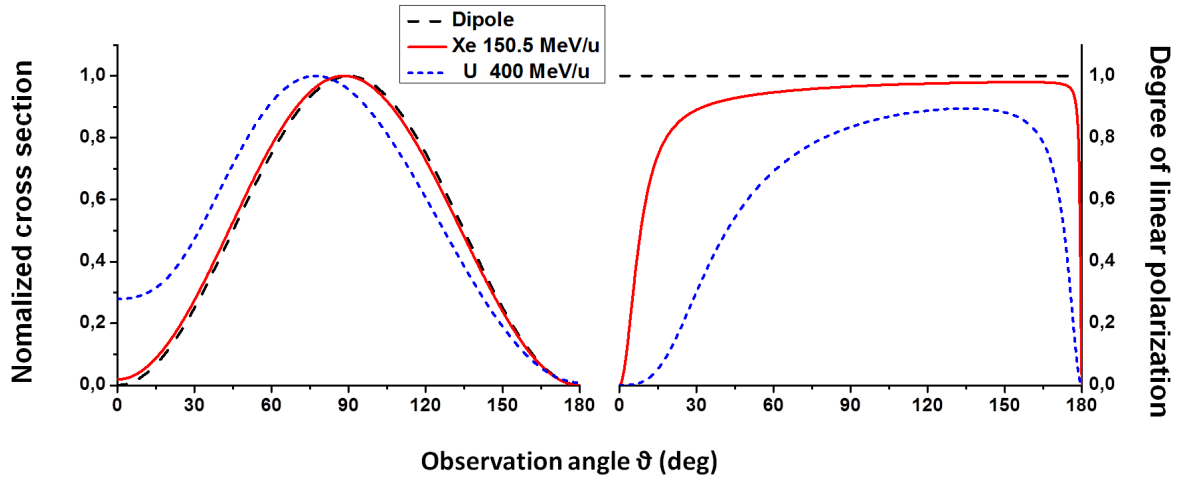


Figure 3.6: Calculated angular distribution and degree of linear polarization of the RR into K-shell of Xe^{54+} with 150.5 MeV/u kinetic energy and U^{92+} with 400 MeV/u kinetic energy, in comparison with the pure non-relativistic dipole characteristics. For the case of Xe, deviation is observable but insignificant, whereas for the case of U, the deviation is severe.

This density-matrix-based formulation is implemented in a Mathematica program by A. Surzhykov et al. [52], which is used for the production of the RR database of the REC calculator that will be introduced in section 5.1. The sample calculations for the experimental condition of this work, i.e. 150.5 MeV/u Xe^{54+} , and for comparison, the case of 400 MeV/u U^{92+} is shown in figure 3.6, where certain deviation from the $\sin^2 \theta$

distributions predicted by the non-relativistic theories can be observed. The predictions about the degree of linear polarization obtained from this fully relativistic theory were tested experimentally, as will be shown in the next chapters.

4 Experimental Study of REC

The underlying measurement campaign of this work was carried out at the GSI Helmholtz center for heavy ion research, one of the biggest research centers in Germany. It was founded in 1969 under the name of Gesellschaft für Schwerionenforschung. The project was triggered by nuclear scientists of the three Hessian universities in Darmstadt, Frankfurt and Marburg due to the strong desire for a central facility in nuclear physics. In 2008 it was renamed as GSI Helmholtzzentrum für Schwerionenforschung GmbH. Today GSI operates a worldwide unique large-scale accelerator facility for heavy ions, which aims for new insights about the building blocks of matter and the evolution of the universe. Based on GSI, the Facility for Antiproton and Ion Research, FAIR, is currently under construction, which will extend the energy range and intensity of ion beams, particularly for short-living isotopes, as well as add a powerful anti-proton production facility [53–55].

This chapter starts with a brief overview of the GSI infrastructures that are relevant to this work. Followed will be a description of experimental techniques and setups.

4.1 Instrumentation – GSI

The backbone of the GSI are the ion acceleration and storage facilities (see figure 4.1), namely the universal linear accelerator (UNILAC), the Schwerionensynchrotron (SIS) and the experimental storage ring (ESR).

4.1.1 Heavy Ion Accelerators

In order to produce highly charged ions, successive collisions with a center-of-mass energy exceeding the binding energy of the to-be-removed electrons are necessary. As an example, for the case of uranium, the heaviest stable element on earth with a K-shell binding energy of about -130 keV. Therefore a minimum of 130 keV of energy should be

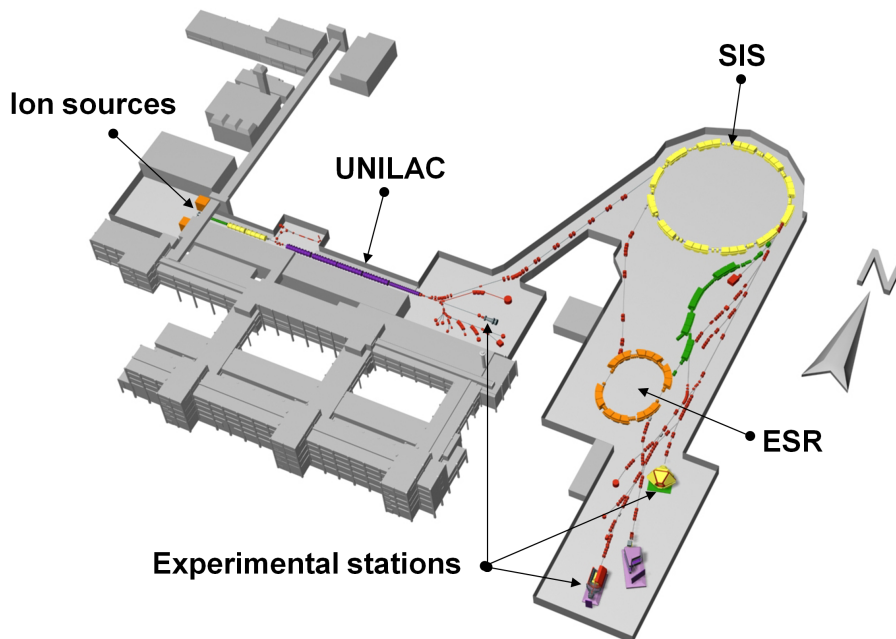


Figure 4.1: Layout of the GSI ion acceleration and storage facilities. Low-charged ions produced at ion sources can be pre-accelerated to about 10% speed of light at UNILAC. Selected ions are injected into the SIS and get further accelerated up to GeV/u of kinetic energy. Finally, the high energy ions are injected into ESR and get stored down and cooled (decelerated if necessary). A variety of physics studies can be carried out at various experimental stations.

transferred during the collision to eject a K-shell electron to generate hydrogen-like or even bare uranium ions.

This can be accomplished either with a relativistic heavy ion beam (with more than 300 MeV/u of kinetic energy) produced in a large accelerator hitting a stationary target (“stripper foil”) as it is done at the GSI accelerators [56], or with an energetic electron beam (with up to 200 keV of kinetic energy and 5000 A/cm² of current density) hitting stationary ions as was done at the Livermore Super-EBIT [57].

In an EBIT, a mixture of various charge states is always present, yet the ion species of interest is not necessarily the most abundant. In contrast, the former method has the

advantage of enabling the production of intense ion beams with only one desired charge state. For this purpose, the two-staged GSI accelerator facility is indispensable.

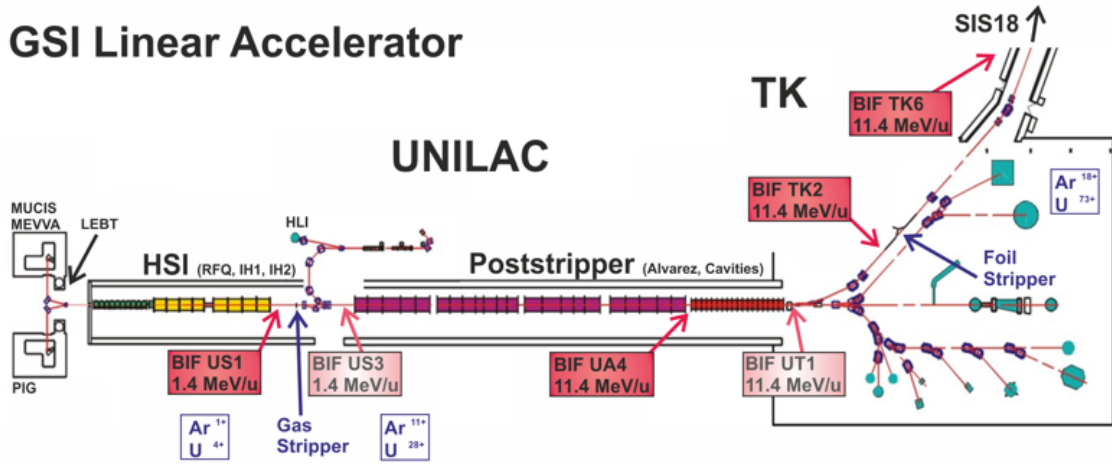


Figure 4.2: Schematic description of the UNILAC: In HSI, low-charge ions are generated by (subsequent) acceleration and stripping in a gas target. Then the ions are accelerated to an energy of 11.4 MeV/u in the poststripper section. After passing through the foil stripper, the ions with desired charge state (typically up to U^{73+}) will be injected into the SIS18.

At first stage, the UNILAC accelerates low-charge ions generated at ion source to an energy of 11.4 MeV/u [58], corresponding to a velocity of about 10 % speed of light. At this energy, U^{73+} can already be produced. After passing through so-called “stripper” target (a thick carbon foil), most of the electrons are ejected due to atomic collisions. The ions with the desired charge state will be magnetically selected out and fed into the SIS for further acceleration (see figure 4.2 for comparison).

Thanks to its 216 m of circumference and 18.7 Tm of magnetic rigidity, the heavy-ion synchrotron, SIS, puts eventually an energy gain of the order of GeV/u to the ions [59]. Through a final stripping and separation in the transfer beamline, bare ions with typical kinetic energy of 400 MeV/u can be produced and then the injected into ESR and stored there for physics studies.

4.1.2 Experimental Storage Ring

If it is the ion accelerators that make study of radiative electron capture (REC) into highly charged ion possible in the first place, it is the experimental storage ring (ESR) that makes it practically feasible (see figure 4.3).

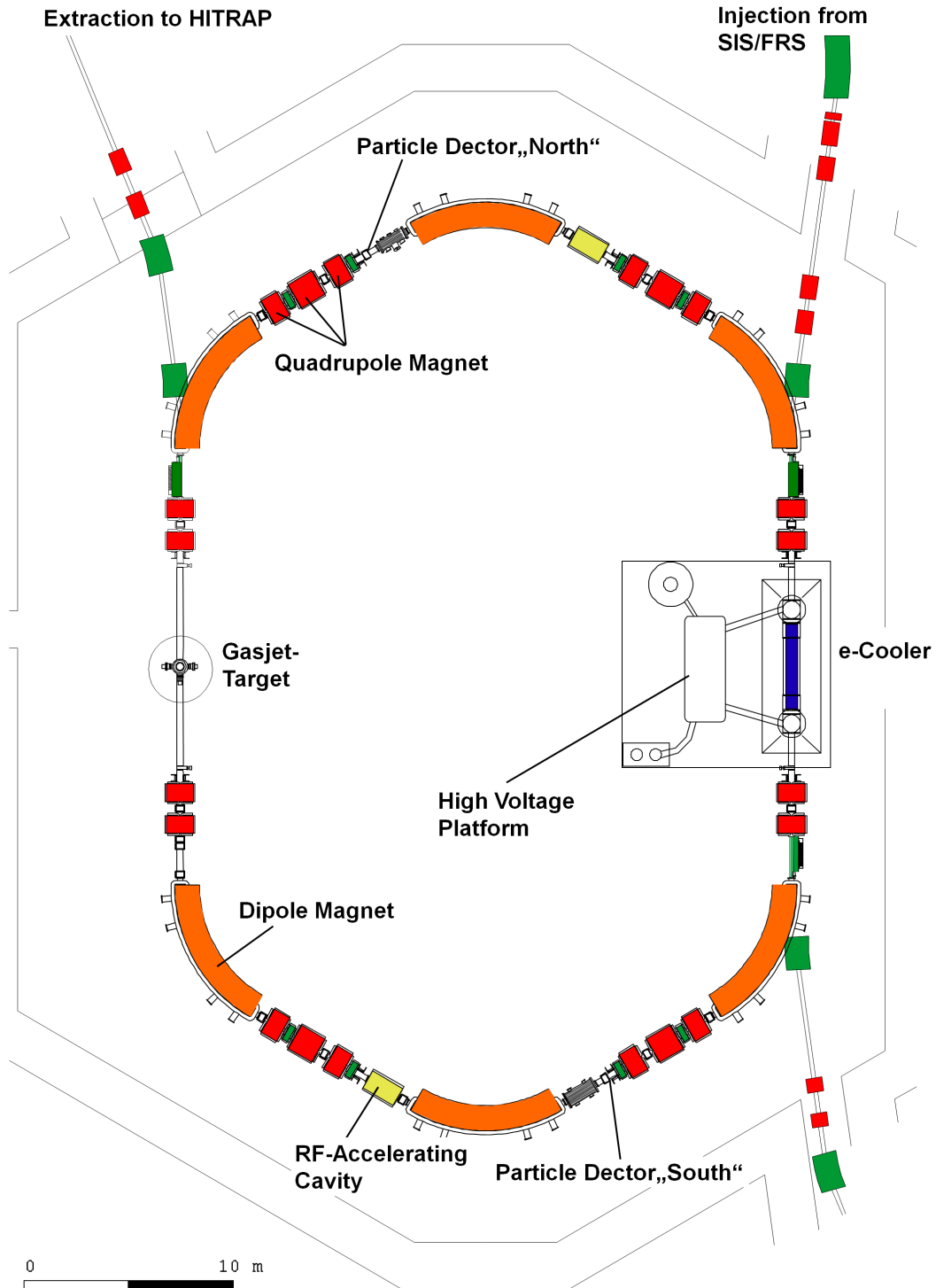


Figure 4.3: Schematics of the experimental storage ring ESR at GSI-Darmstadt. The layout depicts the beam guiding (dipole-, quadrupole magnets), handling system (kicker, RF cavities and electron cooler), diagnostics (Schottky noise pick up) and the internal jet-target.

As the main working horse for atomic physics experiments, the ESR has a circumference of 108 m and a magnetic rigidity of 10 Tm. The geometrical properties together with its ultra high vacuum (UHV) condition (about 10^{-11} mbar of base pressure) allows the ESR to store ions ranging from H^+ to U^{92+} with a typical energy of 5 MeV/u up to approximately 400 MeV/u, with a corresponding revolution rate of the order 10^6 s $^{-1}$ [60].

In the ESR, the initially hot ion beam injected from SIS, with an emittance of about 5π mm mrad, can be cooled through Coulomb collisions with a co-moving cold electron beam in the electron cooler [61] (see figure 4.4). For efficient cooling of higher energy beams (about 400 MeV/u), stochastic cooling is also available [62]. The cooling of the beam reduces the emittance to 0.1π mm mrad or less and provides beam diameters of less than 5 mm. This factor is particularly important for precise measurements at the internal jet target, where a control over geometrical factors and possible Doppler corrections is required. After cooling with a typical electron current between 50 and 250 mA, the relative longitudinal momentum spread $\Delta p/p$ of the ion beam is reduced from approximately 10^{-3} to about 10^{-5} [61].

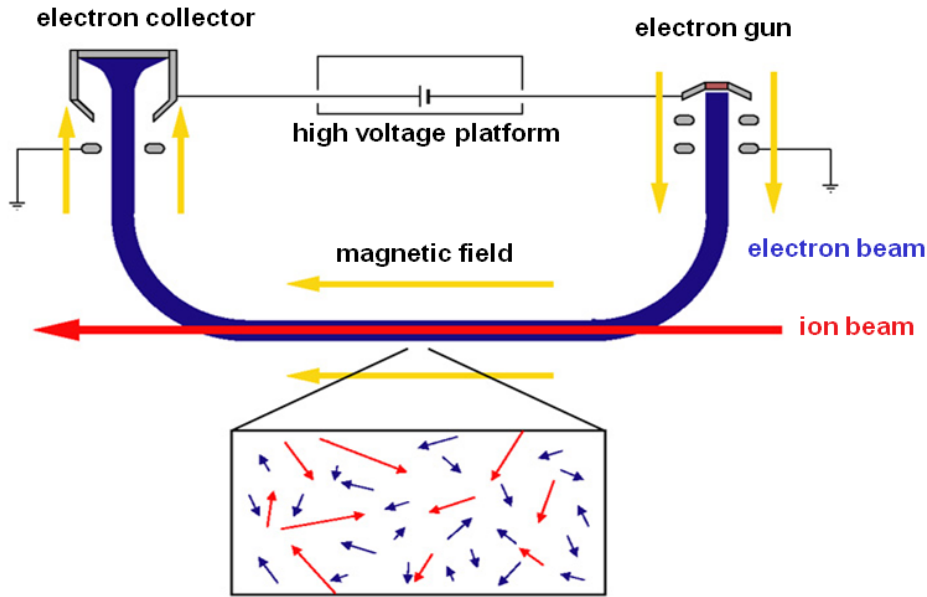


Figure 4.4: Schematic description of the working principle of the electron cooler of the ESR: the characteristics of the cooling beam of electrons (blue) is imprinted on the initially hot ion beam (red) via successive Coulomb collision.

Typical spectra of ion revolution frequencies before/after the cooling is shown in figure 4.5. The data were obtained using the so-called Schottky analysis which is a powerful

tool to monitor the momentum distribution of the ion beam [63]. Besides the improved beam quality, electron cooling offers in the meantime a measure for the velocity of the stored ion, namely, the applied voltage.

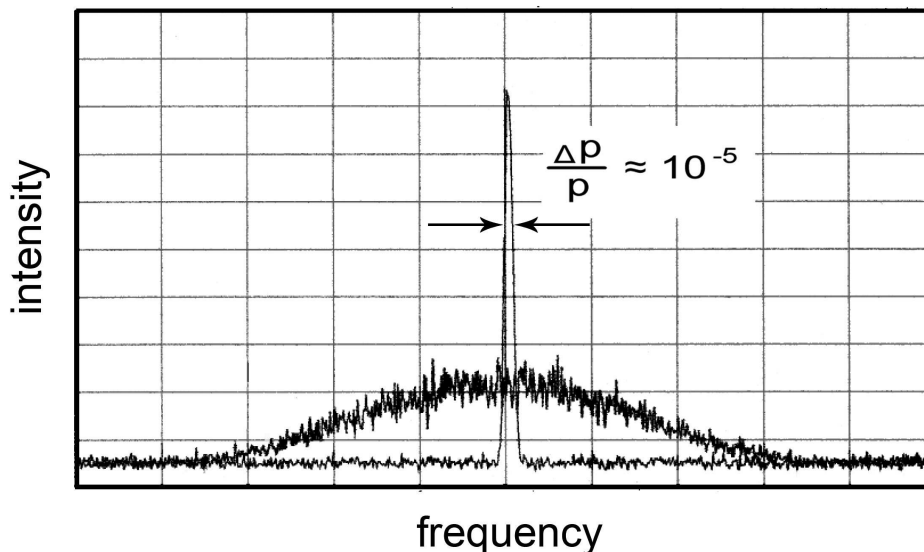


Figure 4.5: Schottky frequency spectrum for a beam of U^{92+} ions at 295 MeV/u. The broad distribution refers to the non-cooled beam, measured directly after injection into the ESR. The narrow distribution reflects the momentum profile of a continuously cooled ion beam [63].

In order to investigate ion-atom collisions in a low energy domain, another unique feature of the ESR, the deceleration capability, can be used. The beam is rebunched and decelerated while the magnetic field is gradually ramped down and the electron cooler is switched off. At the final stage of beam handling, the electron cooler is switched on again to improve the beam quality. In the case of bare uranium ions the lowest beam energy achieved by this procedure is below 10 MeV/u. With the commissioning of HITRAP [64], highly charged ions up to bare uranium at even lower energies (down to at rest are expected) can be studied in precision experiments.

4.1.3 Internal Jet-Target

Many kinds of ion-atom collision phenomena, such as REC, can be studied at ESR's internal jet-target (see figure 4.6), which is designed to produce a uniform target beam consisting of well-defined small clusters (see [65–67] for a detailed description of this target). The target apparatus is divided into several stages where differential pumping

is applied. Despite the formation of a stable gas jet inside the interaction chamber this design preserves the UHV (about 10^{-11} mbar of base pressure) conditions in the ESR.

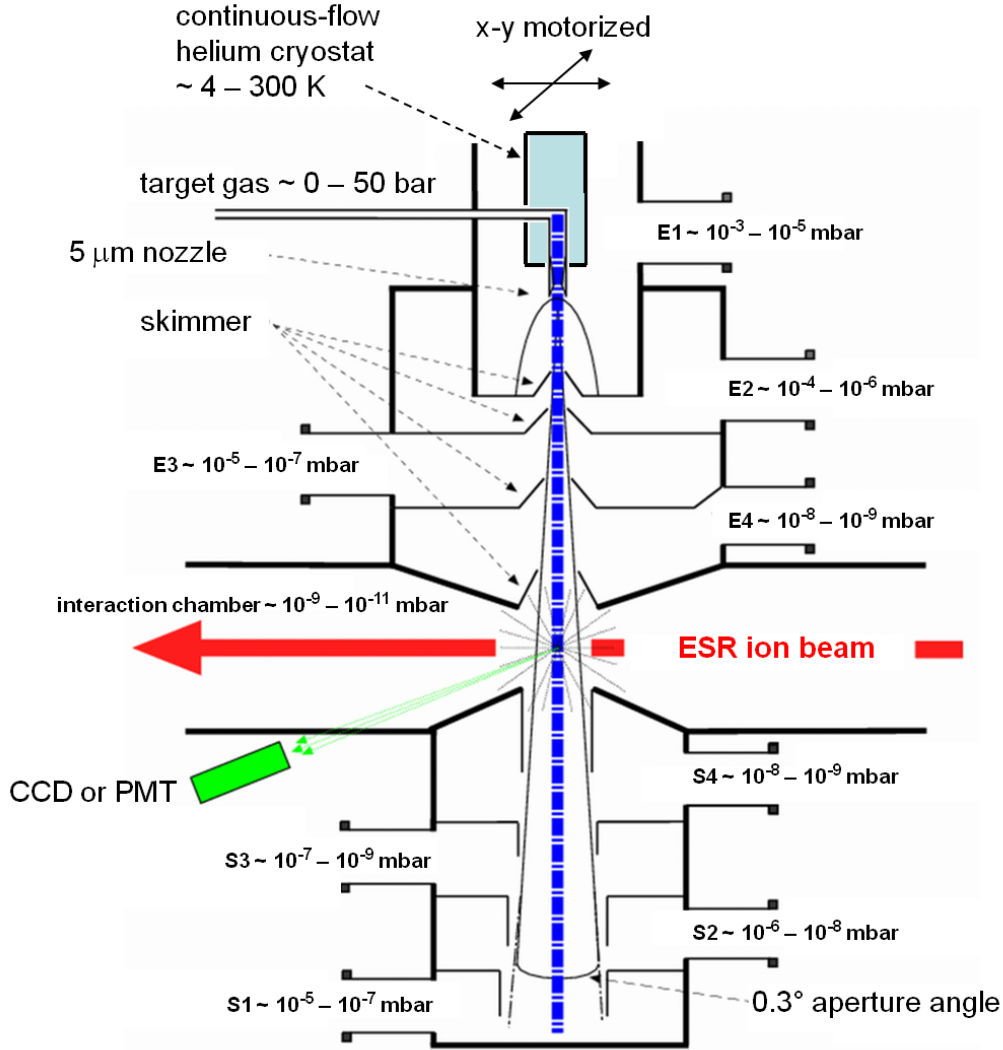


Figure 4.6: Schematic drawing of the internal gas target of the ESR [65].

Target gases currently available are: H_2 , N_2 , Ne , CH_4 , Ar , Kr and Xe . For the expensive noble gases such as krypton or xenon, there is a recycle system available.

By expanding a gas through a Laval nozzle with typical diameters between $50 \mu\text{m}$ and $5 \mu\text{m}$, a target with a typical density of about 10^{13}cm^{-3} (typical density of solid is of order 10^{21}cm^{-3} , for comparison) is produced. When the ion beam circulating in the storage ring pass through the gas target, they collide with the gas atoms. During the collision they can lose or capture electrons and emit X-rays. Note that for atomic physics studies, the gas target mainly serves as a collection of electrons and the rare

interactions of the projectile ions with the nuclei of the target gas are usually not considered. Such a dilute target offers the advantage of minimizing unwanted effects of multiple-collisions which is generally present in high-density solid state targets. Thanks to the high revolution rate (of the order 10^6 s^{-1}), even atomic interactions with small cross sections (0.1 barn [5]) are also experimentally accessible.

The diameter of the target is about 5 mm, measured experimentally via scanning the jet profile by low intensity ion beams with a small beam diameter [66].

At the scattering chamber, the interaction region can be investigated from many different observation angles.

4.2 Experimental Setup

A sketch of the experimental setup for this work is shown in figure 4.7. This setup is especially designed for angular distribution studies of REC. As indicated by the X-ray detectors looking at the interaction region from various observation angles. All detectors are separated from the vacuum environment of the ESR by either stainless steel or beryllium windows with typical thickness of the order $50 \mu\text{m}$. In addition, the dipole magnet analyzes the charge states of the outgoing ion beam so that the X-ray emission can be measured in coincidence with the down-charged projectiles.

An important feature of this setup is the employment of the 2D position-sensitive Si(Li) detector serving as Compton polarimeter (see the subsection 4.2.1 for the details about this detector). With an accurate knowledge about the polarization of the emitted photons more insights can be gained into the REC dynamics.

The possibility to study photon emission close to zero degree is another important feature of the current setup. For this purpose, an intrinsic germanium detector, Ge(i), with four independent segments is mounted on a movable support.

The signals from the pre-amplifiers of the detectors were processed using standard “nuclear instrumental standard” (NIM) and “versa module eurocard” (VME) electronic modules, including timing filter amplifiers (TFA), constant fraction discriminators (CFD), time-to-digital converters (TDC), and analog-to-digital converters (ADC). The resulting data were saved to disk using the list mode data (LMD) format. Detailed descriptions of the setup and the signal analysis modules can be found in the PhD theses by U. Spillmann [68] and S. Hess [69].

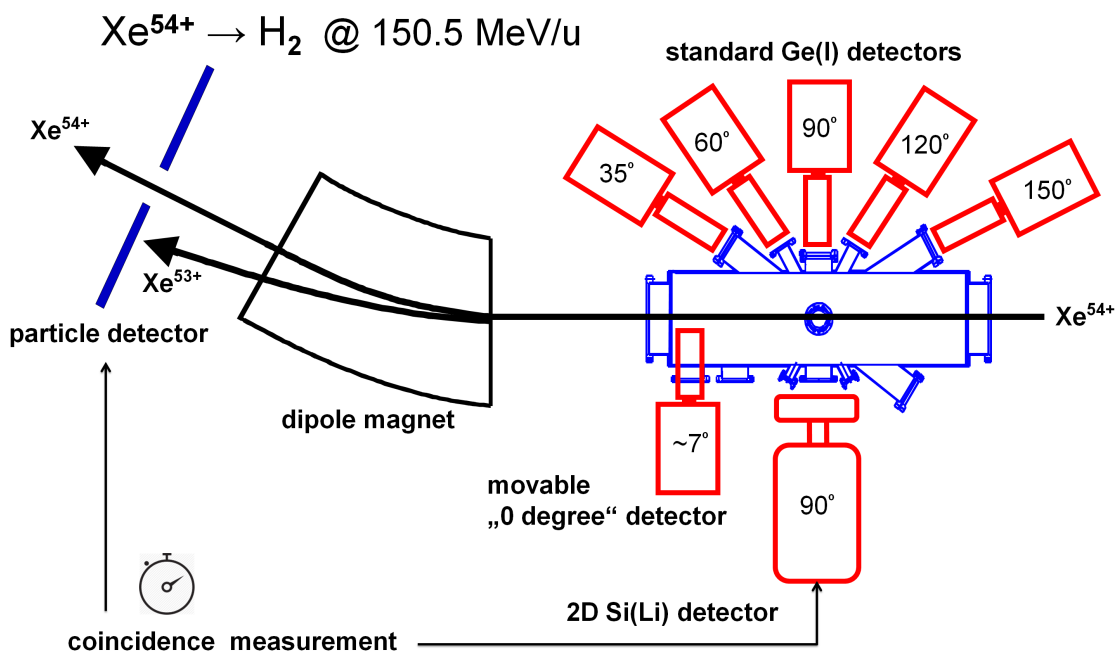


Figure 4.7: Sketch of the experimental setup for a detailed study of the angular distribution and linear polarization of the REC radiation emitted in the capture of electrons into bare xenon ions. Magnetic separation and detection of the down-changed ions provides a coincidence condition for the recorded X-rays leading to a reduction of background radiation.

4.2.1 Si(Li) Polarimeter

Even though first Compton polarimetry measurements using arrays of standard X-ray detectors were performed already since the 1950s [70], efficient, precise and affordable detector systems dedicated for (linear) Compton polarimetry have become available just recently [15, 16], owing to the development of highly segmented solid-state X-ray detectors.

Within the SPARC collaboration [71], a two dimensional position-sensitive detector (see figure 4.8) dedicated for Compton polarimetry was developed and successfully implemented in several experiments [19, 20]. This detector has as sensitive material a

lithium-drifted planar silicon single crystal with a total area of $80 \times 80 \text{ mm}^2$ and a thickness of 7 mm. Each side of the crystal is segmented into 32 strips with 2 mm width of each strip. There are $50 \mu\text{m}$ wide grooves to isolate the segments against each other and the whole active area is surrounded by a guard ring of 7 mm width to drain the leakage currents [16].

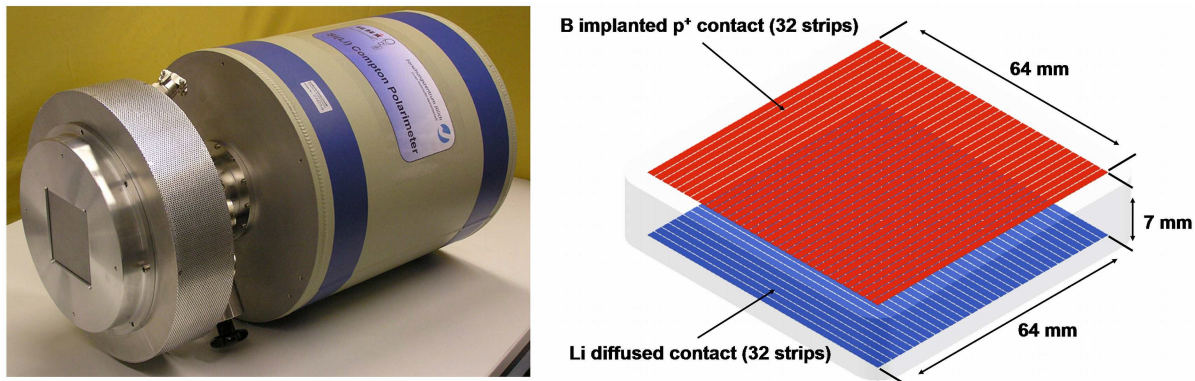


Figure 4.8: Left: Photograph of the Si(Li) Compton polarimeter developed within the SPARC collaboration. The crystal and the preamplifiers are located in the detector head and connected to a LN_2 dewar. Right: Sketch of the detector crystal with the front side and the back side each being segmented into 32 strips giving a structure of 1024 pseudo-pixels.

Each strip is read out independently with a charge sensitive preamplifier providing a time resolution of order 100 ns and a typical energy resolution of 2.5 keV at 100 keV. Moreover, the positive charge carriers are collected in on the front side while the negative carriers on the back. Combining this to the orthogonal orientation of strips on both sides results in total number of 1024 pseudo-pixels with two dimensional position sensitivity, as can be seen from figure 4.8.

It should be pointed out that the experiment presented in this thesis was performed back in 2008 and the data were analyzed then by S. Hess [69]. However, the focus of that work was devoted to the technical challenges in the preparation of the experimental setup with the then newly developed Compton polarimeter, as a result the analysis of the obtained data was preliminary. The data analysis presented in the following chapter, on the other hand, aims to be more precise and sophisticated thanks to the improved methods and the experience gained since 2008.

5 Outcomes of Study

During the period of my master thesis, there are two primary outcomes: One of them is a calculator for REC photon properties; the other is an improved analysis of the REC linear polarization measured with a 2D position sensitive Compton polarimeter. The following sections will be devoted to the presentation and discussion of these results.

5.1 Calculator for REC Cross Section and Polarization

Though the radiative electron capture can be formulated theoretically in a rigorous fashion, the evaluation of the cross sections and polarization properties still relies on numerical computation (c.f. chapter 3 and references [13, 49, 50]). Due to the complexity of the bound-free integral of the electron wavefunctions, such calculations, even for the capture into initially bare ions, are computationally expensive. For example, the time it takes to get convergent results for a reasonable collision energy (e.g. 150.5 MeV/u as in this work), is of the order of a few minutes for a commercially available table-top computer, and that counts only for the recombination into a single orbital of the projectile ion. With increasing collision energies, the time needed will be even longer, as more partial waves are necessary to represent the incident electron (c.f. section 3.3). For instance, a calculation for RR into a single orbital of a projectile with 1 GeV/u of kinetic energy takes about half an hour.

Alternatively, available are tabulated values produced mainly by Eichler and Ichihara et al. [72, 73], where total and angular differential cross sections for many (but not all) elements and collision energies can be found. In practice, however, there are many limitations with these tables. Firstly, the tabulated total cross sections are not for REC but for RR into bare ions. Secondly, one usually does not directly get the cross sections for the required ion species and energies from the papers, especially for the angular distribution where only very limited data sets are given. Though in the original publication there are links to additional supplementary files that provide a much more

comprehensive database, these links to the data repositories are no longer accessible. Ultimately, the polarization properties of the RR/REC photons are not included in the tables at all.

These shortcomings inspired us to create a fast REC calculator, which combines a comprehensive database and a proper interpolation procedure to provide the scientific community an easy access to the angular distribution of REC cross sections and degrees of linear polarization, for almost arbitrary kinematics and observation angles.

5.1.1 Database of Elements

Originally initiated by the need to create a model for the REC photon properties as input for Monte Carlo simulation to improve the understanding of the polarimetric measurements (see subsection 5.2.3), the choice of the projectile atomic number, Z_P , has two aspects of consideration. On one hand, typical projectile choices such as uranium, gold and xenon are included. On the other hand, the Z_P 's to-be-chosen have to homogeneously cover the whole range from 1 to 92 to support the interpolation for an arbitrary Z_P . Consequently, H, N, Ar, Kr, Xe, Dy, Au and U have been chosen as representatives.

At the moment, the database consists of complete sets for the angular differential cross sections and degrees of linear polarization for nine orbitals ($1s_{1/2}$ to $3d_{5/2}$) of each projectile species listed above. For RR/REC into higher orbitals, the spectral lines cannot be resolved by the state-of-art standard X-ray detectors, leading to a quasi-continuous spectral distribution. In a future extension of the REC calculator, this continuum might be modeled by an extrapolation of the trends observed for the angular distribution and the polarization properties of recombination into the lower orbitals.

For each orbital, there are 90 projectile energies between 5 MeV/u and 400 MeV/u, corresponding to the storage capability of the current ESR. An extension of this database to a kinetic energy of 5 GeV/u is in preparation, to accommodate the storage capability of the high energy storage ring (HESR) at the future FAIR facility.

The numerical evaluation of the RR cross section and polarization were performed in a fully relativistic manner using the code provide by A. Surzhykov [52], which is a part of the toolkit DIRAC [74]. The accuracy of the calculation is mainly determined by the accuracy of the continuum wavefunction representing the initial state of the recombined electron, which, during the evaluation, is described by a series expansion in terms of the partial waves (see section 3.3). To this end, one has to carefully choose the number of partial waves, $\nu = 2\kappa_{\max}$, with κ_{\max} being the maximum of the quantum number for the Dirac angular momentum associated with the partial wave, for the expansion: a

too small choice of κ_{\max} may lead to truncation errors; a too large value, on the other hand, may lead to explosion of numerical errors due to the rapid oscillations of the radial part of the continuum wavefunction. With a proper choice of κ_{\max} , an uncertainty of per cent level can be reached for the parameter range concerned in this work [52]. The uncertainty arises from the restrictions of the model, where QED and finite nuclear size and mass are not included.

The computation time is another factor when choosing the partial wave numbers, especially when mass production of data within limited time is necessary. A properly chosen κ_{\max} may reduce significantly the computation time, which scales, roughly speaking, to the third power of κ_{\max} .

In practice, the choice of κ_{\max} was made on a try-and-error basis. Several test calculations were carried out and convergence was judged by comparing the total cross sections with the tabulated values [72]. Due to the lack of both experience and reliable criteria for convergence, my choice of parameters for test calculations were later proven not representative enough. As a consequence, the values of κ_{\max} 's for massive calculation were more on the tend-to-be-small side, which, as will be shown shortly in subsection 5.1.3, limits the reliability of the calculator at relatively high collision energies (about 400 MeV/u). However, it has to be stressed that for the range of projectile energies and ion species that were experimentally studied for this work, the REC calculator has a reliable underlying RR database with an accuracy up to per cent level (see figure 5.1).

Furthermore, due to the absence of QED effects in the model, the energy levels of projectile, in particular the 1s levels of high-Z ions, had systematic discrepancies from the observed spectral lines. In order to correct this inconsistency, the Lamb shift corrections to the Dirac binding energies tabulated by W.R. Johnson and G. Soff [75] were used, for the $1s_{1/2}$ to $3s_{1/2}$ states.

Finally, the impulse approximation (see section 3.1 for more information) was implemented to get the REC spectra, which was realized by folding the RR data with target electron momentum distribution (Compton profile) taken from the tables produced by Biggs et al. [43].

5.1.2 Interpolation Procedure

In general, spline interpolation developed by Akima [76] was applied to obtain RR/REC characteristics in between the rigorously calculated grid points. This method produces a natural-looking curve when it is used for fitting smooth data. However, the Akima method tends to produce undulations when tempting to interpolate nearly straight lines.

For such cases, therefore, a simple linear interpolation procedure was used.

There are, roughly speaking, two steps of interpolation implemented in the calculator.

In the first step, the RR cross section and polarization properties are interpolated with respect to the atomic number of the projectile, Z_P , resulting in the RR data for the required (initially bare) projectile ion with collision energies covering the whole range of the underlying database. Moreover, to create a better shape of curve for the Akima interpolation, the total cross sections are divided by Z_P^5 , while the angular differential cross sections are firstly normalized individually with respect to the maximum of each curve. As for the (angle-dependent) degree of linear polarization, P_L , Akima interpolation was directly applied.

In the second step, REC spectra and polarization properties are produced by convolving the z -projection of target electron momentum profile, i.e. the Compton profile, with the RR data obtained from the previous step using equation (3.6). Particularly, the Compton profile was interpolated with log-log spline fit as function of the longitudinal momentum projection, determined by the photon energy of interest, and the RR data of the projectile ion were interpolated accordingly.

It should be noted that the interpolations were performed in the projectile frame, then the interpolated values were transformed into laboratory frame.

5.1.3 Accuracy of Interpolation

Figure 5.1 depicts the comparison between rigorously calculated (in blue) and interpolated (in pink) K-shell RR angular differential cross sections and degrees of linear polarization in the laboratory frame for various Z_P 's at a collision energy of 200 MeV/u. One can observe that with the increase of Z_P , the cross sections increase whereas the degrees of linear polarization gradually decrease. Most importantly, interpolation of neither cross section nor polarization exhibits significant discrepancy from the rigorously calculated values over almost the whole angular range. Exceptions occur only for observation angles near 180° , where the degrees of polarization drop sharply and a significant deviation is visible. This issue can be solved in the future by an optimized interpolation algorithm for this particular range of observation angles.

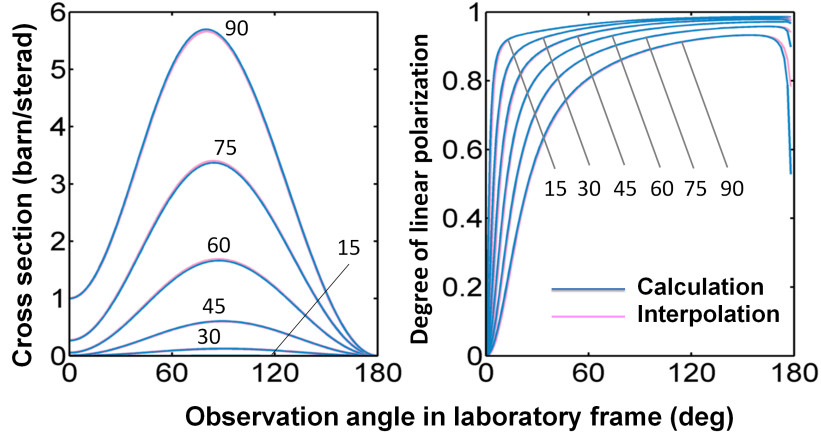


Figure 5.1: Interpolated REC angular differential cross sections and degrees of linear polarization versus the rigorously calculated values for projectile Z_p 's between 15 and 90. The data is given in the laboratory frame. A good agreement is found.

For a quantitative figure of merit, figure 5.2 plots for several collision energies the root-mean-square deviation defined as

$$\Delta_{\text{rms}} = \sqrt{\frac{\sum_{i=1}^N \left(\frac{V_i(i) - V_c(i)}{V_c(i)} \right)^2}{N(N-1)}}, \quad (5.1)$$

where subscripts c and i indicate the values of calculation and interpolation, respectively; summation runs over all sample points of observation angles, which range from 1° to 179° with 1° step size, in the emitter frame.

The relative deviations of the interpolation are generally below per cent level except for the 400 MeV/u case, where a relatively high deviation can be observed. This was caused by the improperly chosen partial wave numbers during the production of database introduced above. It was realized later that this relative deviation can also be used as a criterion for convergence of test calculations, e.g. by comparing the test calculation with $\kappa_{\text{max}} = \kappa$ and that with $\kappa_{\text{max}} = \kappa + 1$, therefore, during the extension of database to 5 GeV/u, a proper choice of partial wave number hence the accuracy of the the RR database can be guaranteed.

Because the REC calculator is able to, up to percent accuracy, resemble the rigorous calculation, its prediction of the photon polarization properties will be taken as the theoretical value and compared with the results of experimental data in the next section.

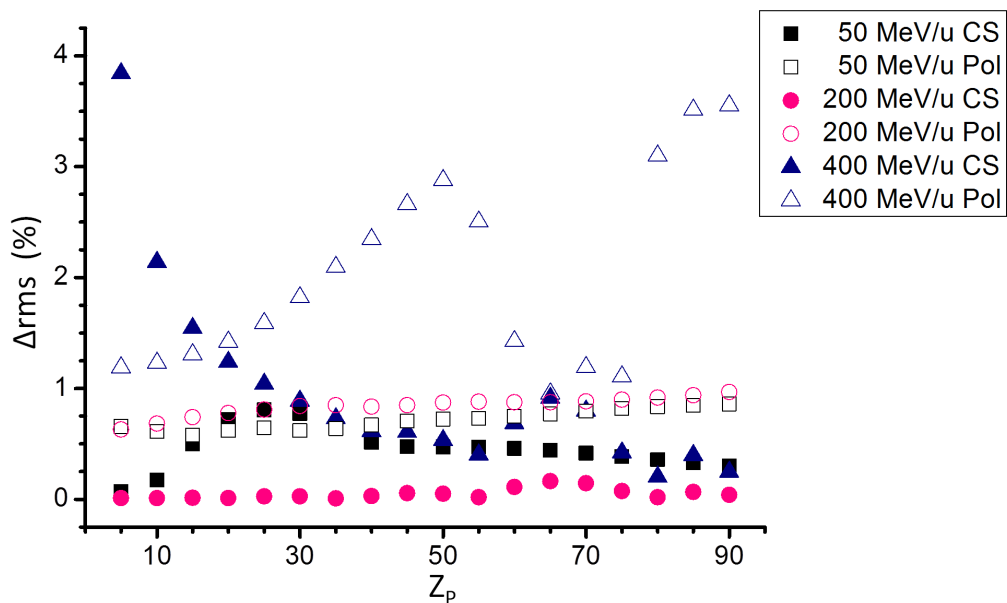


Figure 5.2: The root-mean-square deviation, as a figure of merit, of the interpolated values with respect to the rigorously calculated ones. Solid symbols are for the cross sections whereas the empty ones are for the degrees of linear polarization. The relatively large discrepancies for the 400 MeV/u case are due to the inaccuracy of the RR database caused by the improper choices of partial wave numbers, which will be solved by future calculations, see text for details.

5.2 Linear Polarization of REC Photons

The experimental data obtained with the 2D Si(Li) Compton polarimeter (see figure 4.7 for the details of experimental setups) were analyzed with a program based on SATAN – System to Analyze Tremendous Amounts of Nuclear data [77]. For the purpose of adjusting free parameters of models to fit experimental data, the Fortran-based function minimization routine developed at the CERN, MINUIT [78], was employed. In this section only the results of analysis will be shown, details of the underlying algorithms can be found in the PhD thesis of G. Weber [24].

5.2.1 X-ray Spectrum

Detector Calibration

The energy calibration of the Si(Li) polarimeter was carried out with an Am-241 source and a Eu-152 source, having several well known spectral lines. Therefore the raw spectra

of the calibration sources (figure 5.3) offer the information of the correspondence between the energy deposition in the detector and the analog-to-digital converter channel for each segment of the detector. To be specific, a linear function was adjusted to the calibration data to obtain energy calibration parameters.

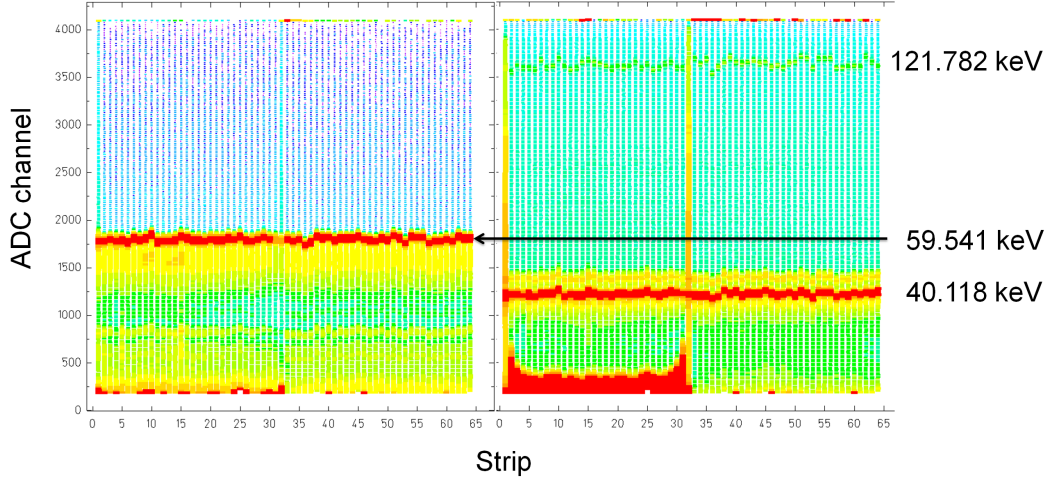


Figure 5.3: Pulse height spectra obtained from calibration sources: on the left is Am-241 and on the right is Eu-152. It can be seen that the first 32 strips (high voltage side of the detector) have a slightly higher noise level than the strips 33 to 64 (ground side).

Correction for Doppler Effect

The calibrated spectra of the X-rays emitted from the interaction of the ion beam with the hydrogen gas target are shown in figure 5.4. One can observe that the strips 0-31, which were oriented parallel to the projectile momentum during the experiment, suffer from Doppler broadening whereas the vertically oriented ones, strips 33-64, Doppler shift. Both features are results of the Lorentz transformation of the photon energies from the reference frame of the relativistic projectile ion into the laboratory system.

With help of the projectile velocity and the position information offered by the segmentation, the above mentioned relativistic Doppler effect can be corrected with the formula

$$\hbar\omega^* = \hbar\omega \frac{1 - \beta \cos \theta}{1 - \beta \cos \theta_{\text{obs}}}, \quad (5.2)$$

where $\hbar\omega^*$ and $\hbar\omega$ are the photon energies after and before correction, respectively; β is the projectile velocity measured in c ; θ and θ_{obs} are respectively the polar angles of the registered event and of the detector centroid, measured in laboratory frame with

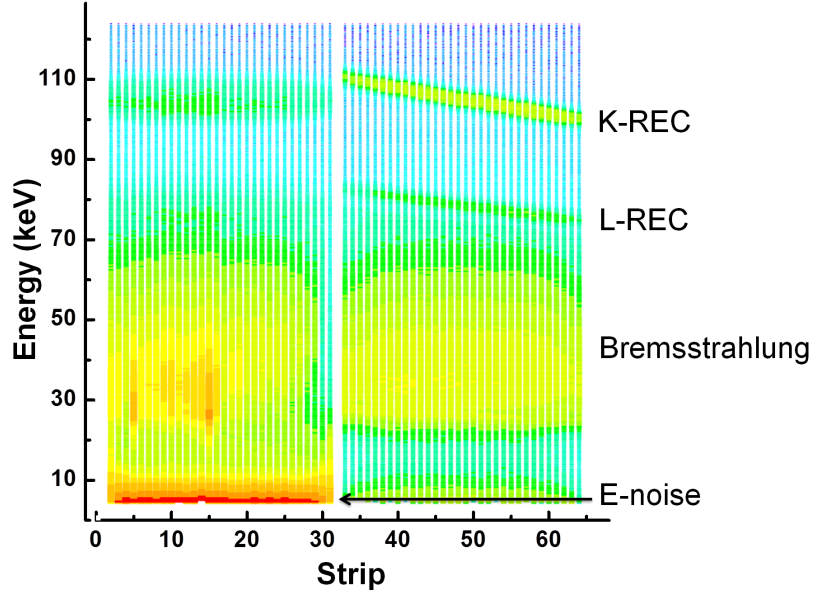


Figure 5.4: The calibrated REC spectra: the horizontally (parallel to projectile momentum) oriented strips (0-31), suffer from Doppler broadening; the vertically oriented ones (33-64) exhibit Doppler shift, as indicated by the variation of peak position among the strips.

respect to the projectile momentum. Note that this correction yields a spectrum for each segment as if it was located in the center of the detector.

Particularly, in order to get the actual polar angle θ , the distance from the detector to the interaction region d , and the central observation angle θ_{obs} , have to be determined accurately (see figure 5.5(a)), since it is calculated with the relation

$$\theta = \theta_{\text{obs}} + \arctan(x/d), \quad (5.3)$$

where x is the relative horizontal position of the event with respect to the detector centroid. It should be noted that a possible rotation of the detector, θ_{rot} , has not been included in the fitting routine yet.

The above mentioned quantities (d and θ_{obs}) were determined by adjusting the Doppler shift of K-REC peaks ($\hbar\omega' = 123.86$ keV in projectile frame) of the vertically aligned strips (strip 33-64, as in figure 5.4) using equation

$$\hbar\omega = \frac{\hbar\omega'}{\gamma(1 - \beta \cos \theta)}, \quad (5.4)$$

where γ is the Lorentz factor of the projectile, as shown in figure 5.5(b).

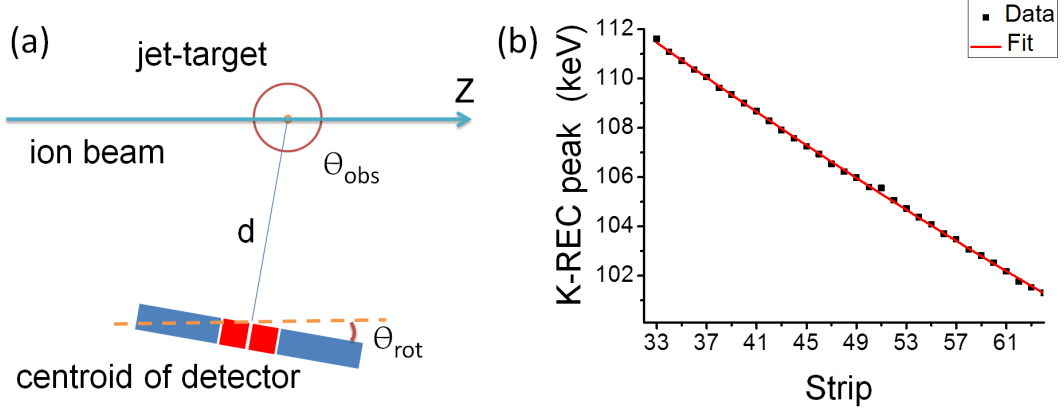


Figure 5.5: (a) Schematic description of the definition of the fitting parameters; (b) Linear fit of the Doppler-shifted K-REC peaks.

After a χ^2 -minimization, the resulting distance from interaction region to detector is

$$d = 32.68 \pm 0.19 \text{ cm}, \quad (5.5)$$

and the central observation angle is

$$\theta_{\text{obs}} = 90.53(2)^\circ, \quad (5.6)$$

with a reduced χ^2 of 0.52. Both quantities are within the expected range determined by the geometry of the target chamber and its view ports.

Single Hit Spectrum

After the correction of Doppler effect, by summing over all the strips and taking into account only the events with multiplicity of one (there is only one energy deposition event at once in the detector), a spectrum as in figure 5.6 is obtained. The restriction of multiplicity selects out mainly the events where the incident photon was absorbed via photoionization and its energy was completely deposited in the detector. Therefore such a single hit spectrum is the best reflection of the spectral characteristics of the incident radiation.

The most prominent feature in this spectrum is the Bremsstrahlung emitted by the free electrons generated during the interaction (ionization of target electrons into the continuum states of the projectile). However, the characteristics of REC together with the geometry of setups (see figure 4.7) allows us to apply a coincidence condition, so

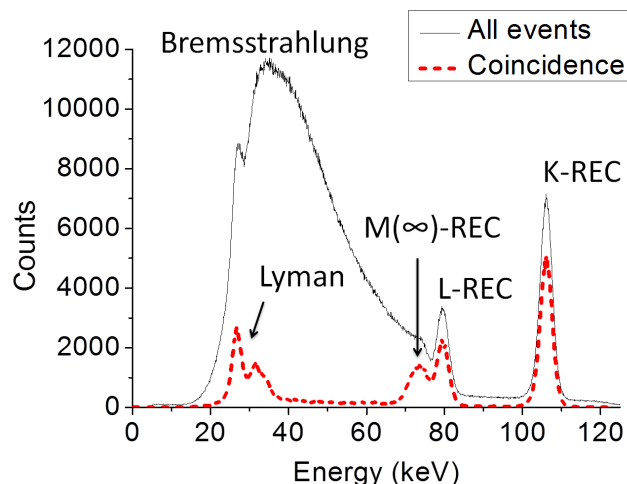


Figure 5.6: Doppler-corrected single hit X-ray spectrum. In the spectrum coincident with down-charged ions (red dotted line), all lines can be attributed to either recombination into the projectile or subsequent characteristics transitions.

that only photons arriving at the detector with a fixed delay with respect to the down-charged ion will be registered, the rather random (lack of correlation to the capture of target electrons) Bremsstrahlung process can be therefore strongly suppressed. Thus an almost background-free spectrum can be obtained where several spectral lines can be readily identified, including the Doppler-shifted REC's from K-shell (at about 106 keV), from the whole L-shell (at about 79 keV), from the M- and all higher shells (at about 74 keV). Also visible are Doppler-shifted Lyman series of the hydrogen-line Xe^{53+} ion (at about 30 keV), which originates from the capture into excited states accompanied by subsequent characteristic transitions. Due to the relative poor energy resolution of the Si(Li) detector, the substructure of the Xe Lyman series can not be distinguished. In the further analysis only the X-rays that are in coincidence with down-charged projectile ions will be investigated. It should be noted that the detection efficiency for the down-charged ions was only about 70% during the experiment. However, the resulting loss of statistical significance for the REC peaks is not crucial.

At this moment, only the spectral lines with energy above about 70 keV can be subject to polarization analysis based on Compton scattering. Because in the Compton analysis, events of interest are the scattering events with longitudinal scattering angle $\theta \approx 90^\circ$ due to the high polarization sensitivity, however, for photons with energies lower than 70 keV, the recoil energy of these events are significantly below 10 keV and hence can not be distinguished from the electronic noise (indicated by the red region near the bottom of figure 5.4) of the preamplifiers that is of the same order of magnitude. When

the electronic noise is not cut-off by a lower threshold, false Compton events might be observed where the recoil electron is in fact a noise signal. On the other hand, true Compton events may get lost because noise signals lead to a wrong estimate of energy deposition within the detector.

With the restriction of photon energy, the K-REC and L-REC lines can be safely analyzed. In the following subsection the K-REC line will be taken as a brief demonstration of the Compton analysis. A more comprehensive description of the analyzing procedure can be found in [24].

5.2.2 Linear Polarization

The starting point of the polarization analysis is the identification of the Compton events that were recorded by the detector: A potential Compton event should meet the minimum requirement that there are two events simultaneously registered in the detector: the recoil electron and the scattered (and then stopped) photon.

For the K-REC at about 106 keV, well below half the rest mass energy of an electron, one can safely identify the event with the smaller energy deposition as the recoil electron and the other as the photon (c.f. subsection 2.2.2). Due to the tiny free path length of the electron, the position where the electron is registered will be taken as the place where the scattering happens. Thus the relative position of the photon with respect to the electron reflects the azimuth angle φ of the Compton scattering. Meanwhile, the polar scattering angle θ can be obtained via the kinematics by solving equation (2.25) for the scattering angle θ as

$$\cos \theta = 1 - \frac{m_e c^2}{E_{\text{ph}}} + \frac{m_e c^2}{E_{\text{ph}} + E_{\text{el}}}. \quad (5.7)$$

A typical scattering intensity distribution together with the corresponding θ distribution can be found in figure 5.7, where only the events with $|\theta - 90^\circ| < 15^\circ$ are shown. Because in this range the azimuth scattering distribution exhibits the highest sensitivity to the incident photon polarization (see section 2.3), plus, the scattered photons have the highest chance to be stopped within the detector.

By binning the counts for different angle φ , the azimuth scattering intensity distribution can be obtained, from which the degree of linear polarization P_L , of the incident beam can be subtracted. It should be already pointed out that if one neglects the actual spatial distribution of events within a pixel and takes simply a delta distribution (at the central point of a pixel for instance) to represent the position, the obtained φ -

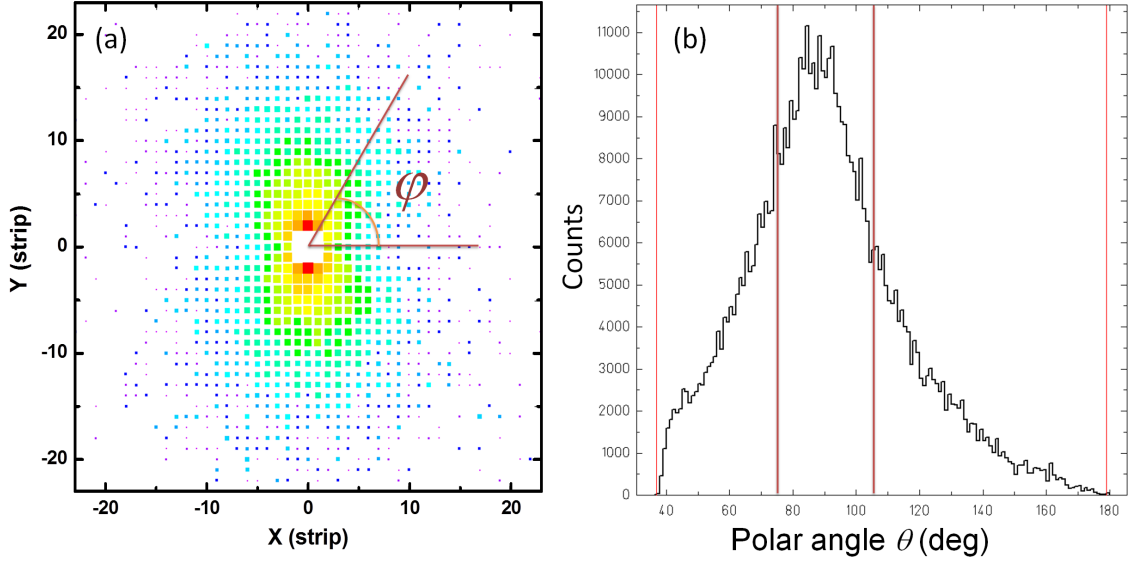


Figure 5.7: (a) Scattering intensity distribution of K-REC photons with an energy of about 106 keV impinging on the Si(Li) polarimeter. (b) The corresponding θ distribution. In the scattering plot, only the events with $|\theta - 90^\circ| < 15^\circ$ are shown, which is marked by the brown lines in the θ plot.

distribution exhibits strong geometrical artefacts, as shown in figure 5.8. Such artefacts can be corrected, to the first order, by smearing the point-like distribution to the whole pixel with a uniform distribution.

Reconstruction of Linear Polarization of Incident Photons

In order to retrieve the degree of the linear polarization from the azimuth distribution of scattering intensity, the Klein-Nishina formula (2.27)

$$\frac{d\sigma}{d\Omega} = \frac{r_e^2 \eta^2}{2} (\eta + \eta^{-1} - 2 \sin^2 \theta \cos^2 \varphi),$$

introduced in section 2.2.2 is taken as a starting point of the fit function:

Firstly, the azimuthal dependence for a single linearly polarized photon in the equation above should be replaced by the expression for a partially polarized photon beam, with the degree of linear polarization being P_L :

$$\cos^2 \varphi \rightarrow (1 - P_L)/2 - P_L \cos^2 \varphi. \quad (5.8)$$

This substitution can be understood as the weighted mean of the contributions from the

non-polarized part, a uniform φ -distribution with height of 1/2, and from the polarized part, a $\cos^2 \varphi$ distribution.

Then the dependence of polar angle θ has to be integrated over the range to be considered to make the function univariate. As the final result, the form of applied fit function can be given as [79]

$$I(\varphi) = B [1 - CP_L \cos(2\varphi - \varphi_0)], \quad (5.9)$$

with the normalization constant for the total spectral intensity

$$B = \frac{I_{\text{tot}}}{N_\varphi}, \quad (5.10)$$

and the modulation depth

$$C = \frac{1}{I_{\text{tot}}} \sum_{\theta} \frac{I(\theta) \eta^2 \sin^3 \theta}{\eta \sin \theta + \eta^3 \sin \theta - \eta^2 \sin^3 \theta}, \quad (5.11)$$

where I_{tot} is the total number of Compton events present in the spatial distribution to be analyzed; N_φ is the number of φ -bins; and $I(\theta)$ corresponds the experimentally measured θ -distribution shown in figure 5.7(b). The parameter ϕ_0 takes into account a possible rotation of the detector about the incident photons' momenta.

By fitting the scattering intensity distribution with equation 5.9, reconstructed degree of linear polarization of the incident photon beam is, P_L^S , is obtained:

$$P_L^S = 0.927 \pm 0.008 \quad (5.12)$$

with a reduced χ^2 of 4.12. Note that here and in the following, only the statistical uncertainty yielded by the minimization algorithm is presented.

This result still suffers from geometrical artefacts due to the lack precise knowledge about the actual position distribution within the finite-sized pixel. Furthermore, the limited energy resolution and many other factors [24] also tend to lower the the anisotropy of the scattering intensity distribution, which results in a quality factor

$$Q = \frac{P_{\text{out}}}{P_{\text{in}}} < 1$$

of the polarimeter. More specifically, the degree of linear polarization obtained by the procedure above is likely to be significantly smaller than the actual degree of polarization

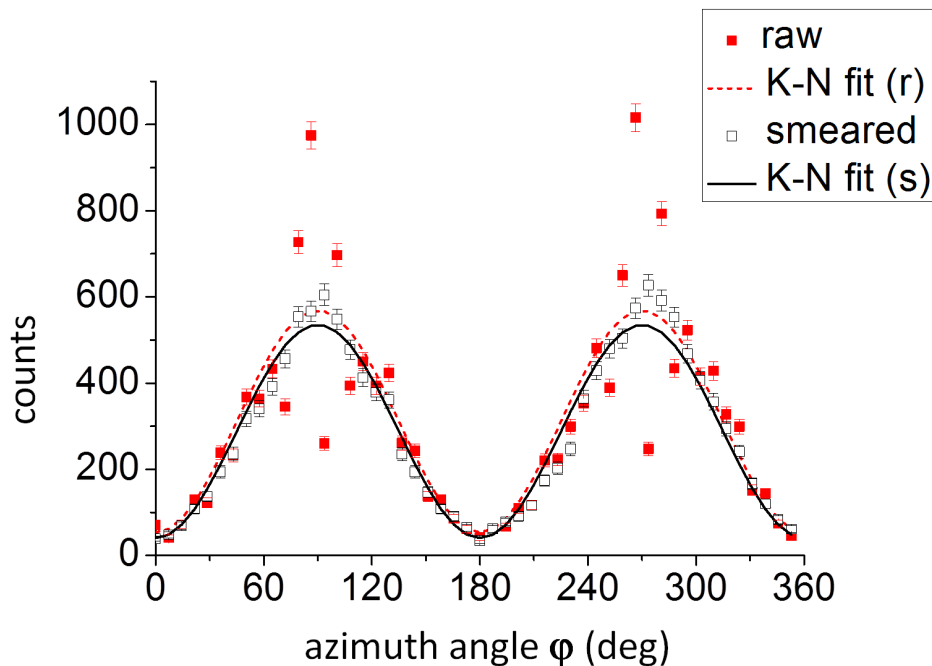


Figure 5.8: Comparison between the Klein-Nishina fits for raw data (red solid square) and smeared data (black empty square). The geometrical artefact – the strong fluctuation of the raw data is significantly reduced by the smearing.

of the incident radiation. In order to get correct interpretation of the measurements, precise knowledge of the quality factor is necessary, which leads to the discussion of the next subsection.

5.2.3 Monte Carlo Simulation

In order to improve the data analysis, the usage of Monte Carlo simulations to model the response function of the polarimeter detector is necessary. Such simulations should lead to a twofold benefits: a correction of geometrical artefacts and other effects in the spatial distribution associated to the detectors properties, and a calibration curve for the polarimeter quality factor.

In this work, the Monte Carlo simulations were performed with the electron gamma shower package, EGS5 [80], which provides the propagation and interaction algorithms for photons and electrons. In addition, the electronic noise and the charge splitting between neighboring segments were included with a simplified model (see references [24, 81] for more information). Moreover, the experimental geometry including the finite size of the interaction zone of gas target and ion beam and the relativistic Doppler shift were also considered. Incident photon properties were calculated with the REC calculator

described in the previous section.

Adjustment of Simulation Parameters

Before any understanding could be gained from the simulation, the parameters in the simulations have to be well adjusted so that the simulations resemble the experimental geometry and detector response, which is ensured by comparing the simulated spectra with the experimental ones.

Figure 5.9(a) shows the comparison between the spectra of the sum-energy of the Compton scattered photon and the recoil electron, zoomed in to the K-REC peak position, and figure 5.9(b) shows the distribution of the polar angle of the Compton events. As can be seen, the simulations reproduce the features of the experimental data hence can be used as orientation for data interpretation.

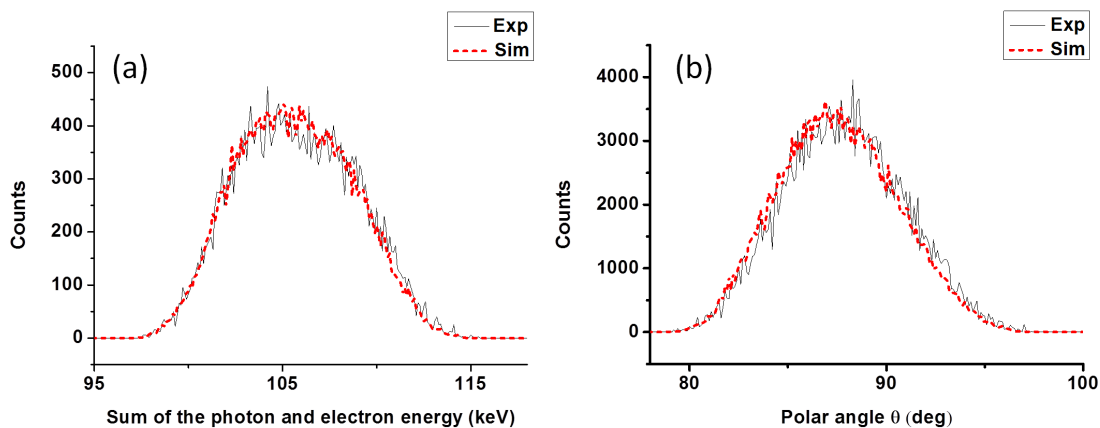


Figure 5.9: Comparison between the experimental and simulated Compton spectra: (a) shows the sum of the photon and electron energy of the reconstructed Compton events; (b) shows the reconstructed polar scattering angle θ .

Normalization of Spatial Distribution of Compton-Scattered Photons

The geometrical artefact presented in figure 5.8 can be suppressed even further by normalizing the experimental scattering pattern to a simulated pattern of a non-polarized but otherwise identical incident radiation. As a result, the degree of linear polarization retrieved from the normalized data is

$$P_L^N = 0.926 \pm 0.008, \quad (5.13)$$

with the reduced χ^2 of 1.89, indicating that the model is more reliable, as can be seen from figure 5.10. The fact that the obtained degree of polarization is nearly identical to the one from equation (5.12) can be attributed to the cancellation of geometrical artefacts as they lead to successive overshoots and undershoots of the intensity compared to the model curve in figure 5.8.

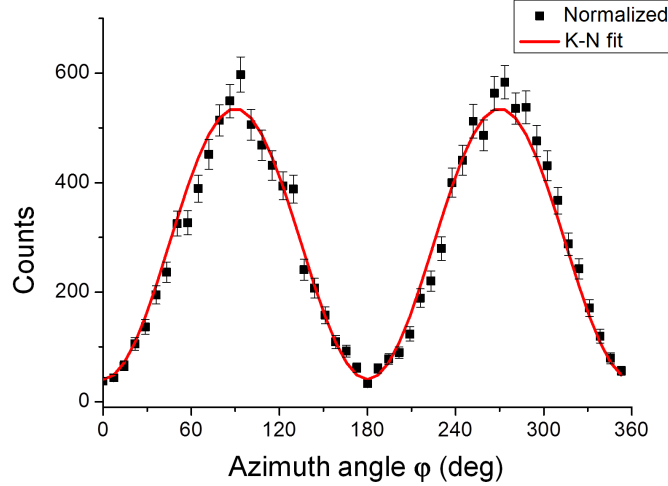


Figure 5.10: Azimuthal distribution of Compton-scattered intensity normalized to the distribution obtained by a Monte Carlo simulation for unpolarized but otherwise identical incident radiation. Geometric artefacts are canceled to a large extent, resulting in a better agreement of the experimental data and the fitting curve with the degree of linear polarization as a free parameter.

Polarimeter Quality Factor

The quality factor of the polarimeter is another important information one can gain from the simulations. By simulating incident radiation with various degrees of linear polarization and process the data with same analysis routine, one obtains, as plotted in figure 5.11, linear fit for the quality factor, which yields

$$Q = 0.974 \pm 0.027. \quad (5.14)$$

Here it is important to note, that the uncertainty of the quality factor is more than three time larger than the statistical uncertainty of the experimental Compton spatial distribution. This large uncertainty is due to the surprisingly large scattering of the reconstructed polarization with respect to the incident polarization for the simulated

data as shown in figure 5.11. Unfortunately, the simulation of one data point takes a day or more on the simulation computer of our group, it was therefore not possible to analyze this issue further during the time of this work. A much smaller uncertainty of the polarimeter quality estimation should be reachable once the problem with the current simulation is identified.

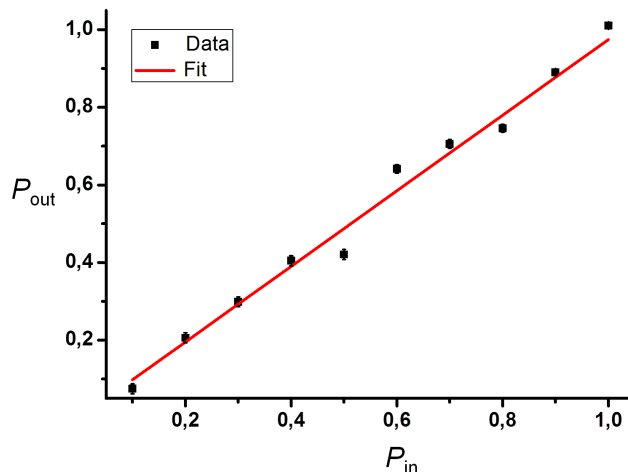


Figure 5.11: Calibration curve for polarimeter quality factor, obtained from simulation of incident radiation with various degrees of linear polarization.

5.2.4 Comparison between Experimental Results and Theory

Combining the degree of linear polarization obtained from data normalization and the quality factor of the polarimeter, the final results of the measured degree of linear polarization of K-shell REC is

$$P_L = \frac{P_L^N}{Q} = 0.950 \pm 0.028. \quad (5.15)$$

As mentioned above, the stated uncertainty is almost exclusively due to the lack of a reliable polarimeter quality estimation, the improvement of which can be achieved by either a more sophisticated model in the Monte Carlo simulation or (possibly) a series of calibration measurements.

This result can be compared with the theoretical prediction of the rigorously calculated RR polarization, or with weighted (by the doubly differential cross section) mean of the polarization curve predicted by the REC calculator. As can be shown by table 5.1, the

Projectile	Experimental Value	Theoretical value	
		REC	RR
Xe ⁵⁴⁺ (150.5 MeV/u)	0.950(28)	0.9602	0.9655

Table 5.1: Comparison between the degrees of linear polarization obtained from the K-REC study and the theoretical values for RR/REC. The difference between RR and REC is due to the fact that for REC one has to integrate over the slightly energy-dependent degrees of polarization of the peak.

results from theory and experiments are, within the uncertainty of the experiment, in agreement.

When compared with the previous results obtained with similar setups [17], the experimental uncertainty is improved by a factor of two to five thanks to the much better position resolution offered by the 1024 pixels (compare with 16 pixels in [17]) of the Si(Li) polarimeter. When compared with the preliminary results from the same measurement by S. Hess [69], the correction of the observation angle and the quality factor (arguably) lead to an improvement of the reliability of the result. Moreover, in the present work, it was possible to take into account the full range of Compton events, while in the previous analysis because of the lack of a proper normalization procedure the data was restricted to a certain range of azimuth angles and distances from the scattering position.

With the analysis routines that were established (or at least improved compared to [24]) in this work, a basis is set to rigorously analyze the data obtained in past experiments with respect to the degree of linear polarization.

6 Additional Experimental Work

Test Measurements of Radiation Yield at High-power Laser Facilities

Besides the radiative electron capture (REC) process in relativistic ion-atom collisions introduced in this thesis, hard X-rays can also arise from plasma interacting with high-power lasers. Detailed study of angular distribution and polarization of laser-generated hard X-ray is desirable and of physics importance. For example, it was recently shown by M. Schnell et al. [82] that the linear polarization of the Betatron radiation emitted by laser-accelerated electron bunches reveals subtle details of the directionality of the laser wakefield dynamics. However, the crystal optics employed in the experimental setup [82] allows polarization analysis only for a dedicated wavelength and for relatively low X-ray energies. Moreover, a recent test experiment by C. Hahn et al. [83] using a Compton polarimeter setup based on CdTe Timepix detectors [84] showed hints for a dependence of hard X-ray polarization emitted from laser-heated plasma on the polarization of the incident laser pulse .

One of the main problems for the implementation of active X-ray detectors (in contrast to passive systems like image plates) at high-power laser environments is the high-flux burst of radiation emitted shortly after the initial laser-matter interaction. In some cases this radiation is also accompanied by powerful electromagnetic pulses (EMP), which can do harm to the readout electronics and computer systems. In order to study these effects, a few test experiments were carried out at two petawatt-class laser systems connected to the Helmholtz-Institute Jena, namely, the POLARIS in Jena, and the PHELIX facility at GSI Darmstadt. In the following I will briefly discuss the experimental setup and the obtained results.

The detector system employed in these experiments consist of four bulks of BC-408 plastic scintillator with volume of $50 \times 11 \times 4 \text{ cm}^3$ of each, coupled along the longest

side via waveguides to EMI-9822B photomultiplier tubes (PMT), biased by a voltage of -2000 V. The voltage signals of the PMTs were read out by a LeCroy wave runner Z66i digital oscilloscope (at PHELIX) or a Tektronix MDO3000 series (at POLARIS). Both oscilloscopes can offer sample rate of more than GS/s, which enables the identification of the signal event even for very high radiation fluxes (the FWHM pulse width of a single event is of the order of 10 ns for comparison).

In the measurement at PHELIX, 500 fs laser pulses with 120 J of energy were focused down to spots with 20 μm in diameter, incident obliquely (72° with respect to target normal) onto a millimeter-thick copper foil (see figure 6.1). Fast target surface electrons (TSE) [85] with up to 10 MeV energy hit the secondary target of aluminium and emitted Bremsstrahlung. The detector system, shield by about 5 cm thick lead, observed the interaction region from 13 meters away backwards of the laser propagation direction. This large distance was necessary to detect reasonable detector signals, because for lower distances the oscilloscope, even though shielded by lead blocks and put into a copper Faraday cage to reduce EMP, produced errors and stopped acquisition.

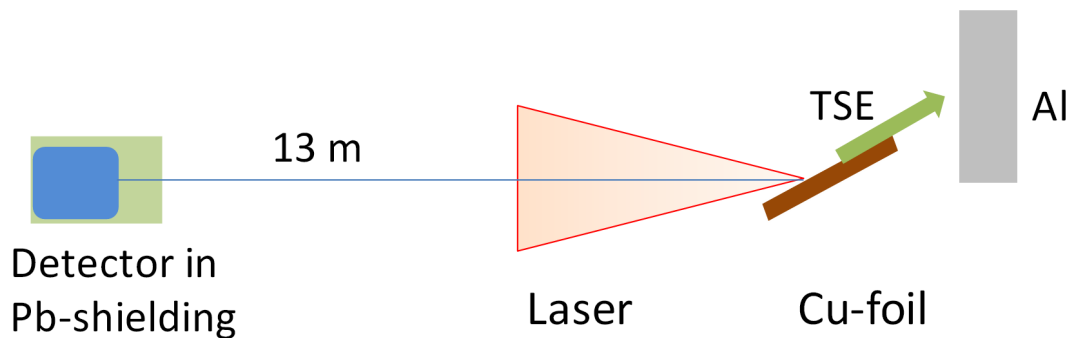


Figure 6.1: Schematic description of the experimental setup at PHELIX laser: 500 fs pulses with 120 J of energy are focused down to spots with 20 μm in diameter, incident obliquely (72° with respect to target normal) onto a millimeter thick copper foil. Detectors are situated 13 meters from the interaction region, shielded by lead blocks.

A typical waveform recorded by the oscilloscope is shown in figure 6.2, where signals of the order of a few volts can be observed (an event caused by cosmic radiation is of the order of 100 mV for comparison). The EMPs caused strong fluctuations of the baseline signal of the PMTs, as a consequence, no isolated event can be identified within this burst. However, by applying a peak finding algorithm to the signal after the initial one microsecond, clear signature of activation was observed, as indicated by the exponential decay of event rate shown in figure 6.3.

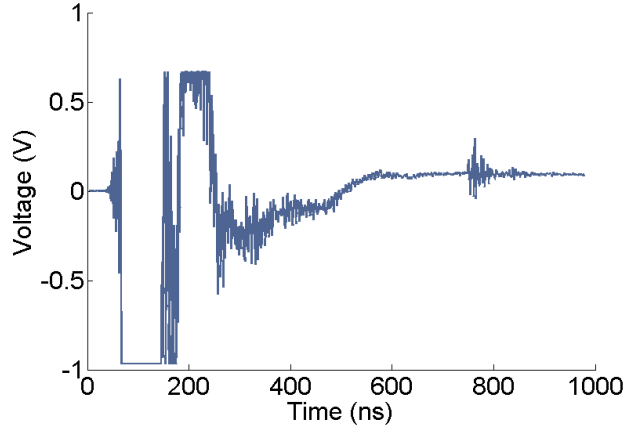


Figure 6.2: A typical waveform recorded by the oscilloscope during the interaction of PHELIX pulse with copper plasma. The volt-order EMP prohibits the identification of isolated events within about $1 \mu s$ after the laser-matter interaction.

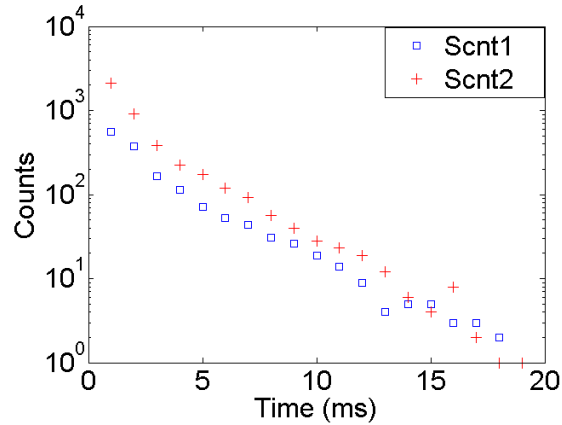


Figure 6.3: Laser-induced activation obtained at the PHELIX facility.

A similar measurement was later performed at POALRIS, where the effects of the initial burst and EMPs were expected not to be vital because of the less energy (about 3.5 J) and less target material (filament consisting of a 50:50 volume mixture of D_2 and H_2). However, as it turned out, there were still overshoots of PMT signal, which blinded the detector for about 100 ns, as shown by figure 6.4. Due to the limited total shot number during the experiment, a conclusion for the observation of neutron generation from D-D fusion can not be drawn as expected.

At this point, we can conclude that the extremely high flux during the laser-matter interaction can be monitored by the above mentioned simple setup; the oscilloscope read-out is robust thanks to the shielding and high output of the PMTs. This radiation could

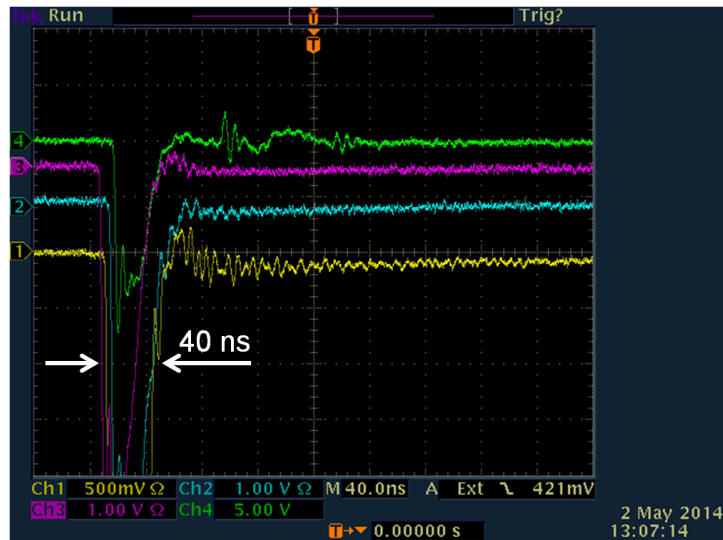


Figure 6.4: Baseline signal distortion of the PMTs during the laser-H(D)₂ filament interaction at the POLARIS laser.

hamper the operation of large-volume active X-ray detectors like the Si(Li) polarimeter introduced in subsection 4.2.1. More sophisticated setups have to be developed in order to make use of such detectors.

7 Summary and Outlook

Within the frame work of my master thesis, the radiative electron capture (REC) was studied with emphasis on the polarization properties.

First, a fast REC calculator was developed, which facilitates the calculation for REC angular differential cross section and degree of linear polarization for initially bare projectiles with kinetic energy between 5 MeV/u and 400 MeV/u. The interpolations of radiative recombination properties performed by this fast calculator are, on the percent level, in agreement with the exact fully relativistic calculations. With the extension of the underlying RR database to 5 GeV/u, this Calculator can be used for the planning and analysis of measurements at the HESR of the future FAIR facility. For example, at the HESR the cross-over of the REC polarization degree to negative values could be studied (c.f. figure 1.2). Moreover, when taking into account the shielding effects, by using the successive ionization approximation and neglecting the electron-electron correlation, the working domain of the calculator could be, in principle, extended to initially hydrogen- or helium-like projectiles.

Second, the data of Xe^{54+} ions colliding with neutral hydrogen gas at 150.5 MeV/u of energy, measured in 2008 using a 2D position sensitive Si(Li) detector, were analyzed with a sophisticated analyzing routine, which yielded results in good agreement with the currently available theory. The K-REC was found strongly polarized at the observation angle near 90° in the laboratory frame, which leads to the potential of tunable polarized hard X-ray source with energy (up to MeV) and degree of linear polarization tunability. The experimental uncertainty arose mainly from the indefiniteness of the quality factor (polarization sensitivity) of the polarimeter, which was estimated using a series of Monte Carlo simulations each requiring a day or more of computation time. Limited by the time frame of this work, a more reliable estimate was not obtained. However, I am optimistic that once this last issue is solved, the present analysis routines can provide a reliable basis for a rigorous final analysis of the available polarimetric data.

Last but not least, additional experimental work addressing the radiation yield arising

from the interaction of high-power lasers with plasmas were performed using plastic scintillators (coupled to PMTs) and a fast multi-channel oscilloscope. It was possible to record the initial radiation burst and also subsequent events due to activation of the experimental setup. The results indicate that the radiation flux in high-power laser environment is much too high to use large-volume, high-stopping power X-ray detectors like the 2D Si(Li) polarimeter.

Bibliography

- [1] J. Eichler and W. Meyerhof, *Relativistic atomic collisions* (Academic Press, 1995).
- [2] N. Stolterfoht, R. D. Rivarola, and R. D. Dubois, *Electron emission in heavy ion-atom collisions* (Springer, 1997).
- [3] E. W. McDaniel, J. B. A. Mitchell, and M. E. Rudd, *Atomic collisions: Heavy-particle projectiles* (John Wiley & Sons, 1993).
- [4] P. Mokler and T. Stöhlker, in *Adv. Atom. Mol. Opt. Phys.* Vol. 37 (Academic Press, 1996), p. 297.
- [5] J. Eichler and T. Stöhlker, *Phys. Rep.* **439**, 1 (2007).
- [6] T. Stöhlker, T. Ludziejewski, F. Bosch, R. Dunford, C. Kozhuharov, P. Mokler, H. Beyer, O. Brinzaescu, B. Franzke, J. Eichler, A. Griegal, S. Hagmann, A. Ichihara, A. Krämer, J. Lekki, D. Liesen, F. Nolden, H. Reich, P. Rymuza, Z. Stachura, M. Steck, P. Swiat, and a. Warczak, *Phys. Rev. Lett.* **82**, 3232 (1999).
- [7] A. Gumberidze, T. Stöhlker, D. Banaś, K. Beckert, P. Beller, H. F. Beyer, F. Bosch, S. Hagmann, C. Kozhuharov, D. Liesen, F. Nolden, X. Ma, P. H. Mokler, M. Steck, D. Sierpowski, and S. Tashenov, *Phys. Rev. Lett.* **94**, 223001 (2005).
- [8] S. Chatterjee, H. Beyer, D. Liesen, T. Stöhlker, A. Gumberidze, C. Kozhuharov, D. Banas, D. Protic, K. Beckert, P. Beller, T. Krings, F. Bosch, B. Franzke, S. Hagmann, J. Hoszowska, P. Indelicato, H.-J. Kluge, X. Ma, B. Manil, I. Mohos, F. Nolden, U. Popp, A. Simionovici, D. Sierpowski, M. Steck, U. Spillmann, C. Brandau, E. Förster, Z. Stachura, S. Tashenov, M. Trassinelli, A. Warczak, O. Wehrhan, E. Ziegler, S. Trotsenko, and R. Reuschl, *Nucl. Instrum. Meth. Phys. Res., Sect. B* **245**, 67 (2006).

- [9] T. Stöhlker, H. Reich, K. Beckert, F. Bosch, A. Gallus, H. Eickhoff, B. Franzke, T. Kandler, O. Klepper, C. Kozhuharov, G. Menzel, P. Mokler, F. Nolden, H. Prinz, P. Spädtke, M. Steck, T. Winkler, R. Dunford, P. Rymuza, T. Ludziejewski, Z. Stachura, P. Swiat, and A. Warczak, *Hyperfine Interact.* **108**, 29 (1997).
- [10] M. Trassinelli, A. Kumar, H. F. Beyer, P. Indelicato, R. Märtin, R. Reuschl, Y. S. Kozhedub, C. Brandau, H. Bräuning, S. Geyer, A. Gumberidze, S. Hess, P. Jagodzinski, C. Kozhuharov, D. Liesen, U. Spillmann, S. Trotsenko, G. Weber, D. F. A. Winters, and T. Stöhlker, *Europhys. Lett.* **87**, 63001 (2009).
- [11] T. Ludziejewski, T. Stöhlker, S. Keller, H. Beyer, F. Bosch, O. Brinzaescu, R. W. Dunford, B. Franzke, C. Kozhuharov, D. Liesen, A. E. Livingston, G. Menzel, J. Meier, P. H. Mokler, H. Reich, P. Rymuza, Z. Stachura, M. Steck, L. Stenner, P. Swiat, and A. Warczak, *J. Phys. B* **31**, 2601 (1998).
- [12] M. Nofal, S. Hagmann, T. Stöhlker, D. H. Jakubassa-Amundsen, C. Kozhuharov, X. Wang, A. Gumberidze, U. Spillmann, R. Reuschl, S. Hess, S. Trotsenko, D. Banas, F. Bosch, D. Liesen, R. Moshhammer, J. Ullrich, R. Dörner, M. Steck, F. Nolden, P. Beller, H. Rothard, K. Beckert, and B. Franczak, *Phys. Rev. Lett.* **99**, 163201 (2007).
- [13] A. Ichihara, T. Shirai, and J. Eichler, *Phys. Rev. A* **49**, 1875 (1994).
- [14] R. Kroeger, W. Johnson, J. Kurfess, and B. Philips, *Nucl. Instr. Meth. Phys. Res., Sect. A* **436**, 165 (1999).
- [15] U. Spillmann, H. Bräuning, S. Hess, H. Beyer, T. Stöhlker, J.-C. Dousse, D. Protic, and T. Krings, *Rev. Sci. Instrum.* **79**, 083101 (2008).
- [16] G. Weber, H. Bräuning, S. Hess, R. Märtin, U. Spillmann, and T. Stöhlker, *J. Instr.* **5**, C07010 (2010).
- [17] S. Tashenov, T. Stöhlker, D. Banaś, K. Beckert, P. Beller, H. F. Beyer, F. Bosch, S. Fritzsche, A. Gumberidze, S. Hagmann, C. Kozhuharov, T. Krings, D. Liesen, F. Nolden, D. Protic, D. Sierpowski, U. Spillmann, M. Steck, and A. Surzhykov, *Phys. Rev. Lett.* **97**, 223202.
- [18] F. Sauter, *Ann. Phys.* **11**, 454 (1931).
- [19] G. Weber, H. Bräuning, A. Surzhykov, C. Brandau, S. Fritzsche, S. Geyer, S. Hagmann, S. Hess, C. Kozhuharov, R. Märtin, N. Petridis, R. Reuschl, U. Spillmann, S. Trotsenko, D. F. A. Winters, and T. Stöhlker, *Phys. Rev. Lett.* **105**, 243002 (2010).

-
- [20] R. Märtin, G. Weber, R. Barday, Y. Fritzsche, U. Spillmann, W. Chen, R. D. DuBois, J. Enders, M. Hegewald, S. Hess, A. Surzhykov, D. B. Thorn, S. Trotsenko, M. Wagner, D. F. A. Winters, V. A. Yerokhin, and T. Stöhlker, *Phys. Rev. Lett.* **108**, 264801 (2012).
- [21] H. Bräuning, S. Hess, S. Geyer, U. Spillmann, C. Kozhuharov, T. Krings, A. Kumar, R. Märtin, D. Protic, R. Reuschl, M. Trassinelli, S. Trotsenko, G. Weber, D. Winters, and T. Stöhlker, *AIP Conf. Proc.* **1099**, 117 (2009).
- [22] S. Hess, H. Bräuning, U. Spillmann, C. Brandau, S. Geyer, S. Hagmann, M. Hege-
wald, C. Kozhuharov, T. Krings, A. Kumar, R. Märtin, D. Protic, B. O'Rourke, R.
Reuschl, M. Trassinelli, S. Trotsenko, G. Weber, D. F. A. Winters, and T. Stöhlker,
J. Phys.: Conf. Ser. **163**, 012072 (2009).
- [23] S. Hess, H. Bräuning, U. Spillmann, S. Geyer, S. Hagmann, C. Kozhuharov, T.
Krings, A. Kumar, R. Märtin, B. E. O'Rourke, R. Reuschl, S. Trotsenko, G. Weber,
D. Winters, and T. Stöhlker, *J. Phys: Conf. Ser.* **194**, 012025 (2009).
- [24] G. Weber, *Untersuchung zur Anisotropie und linearen Polarisation radiativer
Prozesse in energiereichen Ion-Atom-Stößen*, PhD. thesis Ruprecht-Karls-Universität
Heidelberg, (2010).
- [25] C. Cohen-Tannoudji, B. Diu, and F. Laloë, *Quantum mechanics* (Wiley, 1977).
- [26] K. Blum, *Density matrix theory and applications* (Springer, 1996).
- [27] P. E. Kaaret, R. Novick, C. Martin, P.-S. Shaw, T. Hamilton, R. Sunyaev, I. Y.
Lapshov, E. H. Silver, M. C. Weisskopf, R. F. Elsner, G. A. Chanan, E. Costa,
G. Manzo, G. W. Fraser, and G. C. Perola, *Opt. Eng.* **29**, 773 (1990).
- [28] Q. Shen and K. D. Finkelstein, *Phys. Rev. B* **45**, 5075 (1992).
- [29] E. Meltchakov, H. C. Mertins, M. Scheer, S. D. Fonzo, W. Jark, and F. Schfers, *J.
of Magn. Magn. Mat.* **240**, 550 (2002).
- [30] R. Bellazzini, G. Spandre, M. Minuti, L. Baldini, A. Brez, F. Cavalca, L. Latronico,
N. Omodei, M. Razzano, F. Angelini, M. Massai, C. Sgr, E. Costa, and P. Soffitta,
Nucl. Instr. Meth. Phys. Res., Sect. A **576**, 183 (2007).
- [31] B. Wojtsekhowski, D. Tedeschi, and B. Vlahovic, *Nucl. Instr. Meth. Phys. Res.,
Sect. A* **515**, 605 (2003).
- [32] R. A. Sareen, W. Urban, A. R. Barnett, and B. J. Varley, *Rev. Sci. Instrum.* **66**,
3653 (1995).

- [33] F. Lei, A. Dean, and G. Hills, *Space Sci. Rev.* **82**, 309 (1997).
- [34] P. Soffitta, L. Baldini, R. Bellazzini, A. Brez, E. Costa, G. D. Persio, L. Latronico, N. Omodei, L. Pacciani, and G. Spandre, *Nucl. Instr. Meth. Phys. Res. A* **510**, 170 (2003).
- [35] J. West and J. Morton, *Atom. Data Nucl. Data Tables* **22**, 103 (1978).
- [36] W. Leo, *Techniques for nuclear and particle physics experiments: a how-to approach* (Springer, 1994).
- [37] *XCOM: Photon Cross Sections Database*,
<http://physics.nist.gov/PhysRefData/Xcom/Text/XCOM.html>.
- [38] A. H. Compton, *Phys. Rev.* **21**, 483 (1923).
- [39] O. Klein and Y. Nishina, *Z. Physik* **52**, 853 (1929).
- [40] K. Hino and T. Watanabe, *Phys. Rev. A* **36**, 581 (1987).
- [41] K. Hino and T. Watanabe, *Phys. Rev. A* **39**, 3373 (1989).
- [42] E. Clementi and C. Roetti, *Atomic Data and Nuclear Data Tables* **14**, 177 (1974).
- [43] F. Biggs, L. Mendelsohn, and J. Mann, *Atom. Data and Nucl. Data Tables* **16**, 201 (1975).
- [44] T. Surić, *Nucl. Instr. Meth. Phys. Res., Sect. A* **314**, 240 (1992).
- [45] F. Coester, *Phys. Rev.* **84**, 1259 (1951).
- [46] P. Dirac, *The principles of quantum mechanics, 4th edition* (Oxford University Press, Oxford, 1958).
- [47] E. Spindler, H. D. Betz, and F. Bell, *Phys. Rev. Lett.* **42**, 832 (1979).
- [48] M. Stobbe, *Ann. Phys. (Leipzig)* (1930).
- [49] A. Surzhykov, S. Fritzsche, and T. Stöhlker, *Phys. Lett. A* **289**, 213 (2001).
- [50] A. Surzhykov, S. Fritzsche, T. Stöhlker, and S. Tashenov, *Phys. Rev. A* **68**, 022710 (2003).
- [51] J. Eichler, A. Ichihara, and T. Shirai, *Phys. Rev. A* **58**, 2128 (1998).
- [52] A. Surzhykov, *private communication*, (2014).
- [53] W. Henning, *AIP Conf. Proc.* **773**, 3 (2005).
- [54] P. Spiller and G. Franchetti, *Nucl. Instr. Meth. Phys. Res., Sect. A* **561**, 305 (2006).

- [55] W. F. Henning, Nucl. Phys. A **805**, 502c (2008).
- [56] C. Scheidenberger, T. Stöhlker, W. Meyerhof, H. Geissel, P. Mokler, and B. Blank, Nucl. Instr. Meth. Phys. Res., Sect. B **142**, 441 (1998).
- [57] R. E. Marrs, S. R. Elliott, and D. A. Knapp, Phys. Rev. Lett. **72**, 4082 (1994).
- [58] W. Barth, L. Dahl, J. Glatz, L. Groening, S. Richter, and S. Yaramishev, in Proceedings of EPAC 2004, Lucerne, Switzerland (2004).
- [59] D. Böhne, K. Blasche, B. Franczak, B. Franzke, H. Prange, and R. Steiner, in Proceedings of EPAC 90, Nice, France (1990).
- [60] B. Franzke, Nucl. Instr. Meth. Phys. Res., Sect. B **24-25**, 18 (1987).
- [61] M. Steck, P. Beller, K. Beckert, B. Franzke, and F. Nolden, Nucl. Instr. Meth. Phys. Res., Sect. A **532**, 357 (2004).
- [62] F. Nolden, K. Beckert, F. Caspers, B. Franczak, B. Franzke, R. Menges, A. Schwinn, and M. Steck, Nucl. Instr. Meth. Phys. Res., Sect. A **441**, 219 (2000).
- [63] B. Schlitt, K. Beckert, T. Beha, H. Eickhoff, B. Franzke, H. Geissel, H. Irnich, H. Jung, T. Kerscher, O. Klepper, K. Lbner, G. Münzenberg, F. Nolden, Y. Novikov, T. Radon, H. Reich, A. Schwinn, M. Steck, K. Sümmerer, T. Winkler, and H. Wollnik, Hyperfine Interact. **99**, 117 (1996).
- [64] F. Herfurth, T. Beier, L. Dahl, S. Eliseev, S. Heinz, O. Kester, C. Kozhuharov, G. Maero, and W. Quint, Int. J. Mass Spectr. **251**, 266 (2006).
- [65] H. Reich, W. Bourgeois, B. Franzke, A. Kritzer, and V. Varentsov, Nucl. Phys. A **626**, 417 (1997).
- [66] A. Krämer, A. Kritzer, H. Reich, and T. Stöhlker, Nucl. Instr. Meth. Phys. Res., Sect. B **174**, 205 (2001).
- [67] M. Kühnel, N. Petridis, D. Winters, U. Popp, R. Dörner, T. Stöhlker, and R. Grisenti, Nucl. Instr. Meth. Phys. Res., Sect. A **602**, 311 (2009).
- [68] U. Spillmann, *Charakterisierung und erster experimenteller Einsatz von ortsauflösenden, energiedispersiven Germanium-Detektoren zur Präzisionspektroskopie an schweren Ionen*, PhD. thesis Johann-Wolfgang-Goethe-Universität Frankfurt, (2009).
- [69] S. Hess, *Compton-Polarimetrie mit ortsauflösenden Röntgendetektoren*, PhD. thesis Johann-Wolfgang-Goethe-Universität Frankfurt, (2010).
- [70] F. Metzger and M. Deutsch, Phys. Rev. **78**, 551 (1950).

- [71] *SPARC–Stored Particle Atomic Physics Research Collaboration*,
<https://www.gsi.de/sparc>.
- [72] A. Ichihara and J. Eichler, *Atom. Data Nucl. Data Tables* **74**, 1 (2000).
- [73] A. Ichihara and J. Eichler, *Atom. Data Nucl. Data Tables* **79**, 187 (2001).
- [74] S. McConnell, S. Fritzsche, and A. Surzhykov, *Comp. Phys. Comm.* **181**, 711 (2010).
- [75] W. Johnson and G. Soff, *Atom. Data Nucl. Data Tables* **33**, 405 (1985).
- [76] H. Akima, *ACM Trans. Math. Softw.* **17** (1991).
- [77] *SATAN/GRAF*,
<http://www-wnt.gsi.de/CHARMS/SATAN/graf.htm>.
- [78] *MINUIT*,
<http://wwwasdoc.web.cern.ch/wwwasdoc/minuit/minmain.html>.
- [79] K.-H. Blumenhagen, *private communication*, (2014).
- [80] H. Hirayama, Y. Namito, A. F. Bielajew, S. J. Wilderman, and W. R. Nelson, *The EGS5 Code System. Report SLAC-R-730*, Stanford Linear Accelerator Center (2005).
- [81] G. Weber, H. Bräuning, R. Märtin, U. Spillmann, and T. Stöhlker, *Phys. Scr.* **2011**, 014034 (2011).
- [82] M. Schnell, A. Sävert, I. Uschmann, M. Reuter, M. Nicolai, T. Kämpfer, B. Landgraf, O. Jäckel, O. Jansen, A. Pukhov, M. C. Kaluza, and C. Spielmann, *Nat. Comm.* **4**, 2421 (2013).
- [83] C. Hahn, in *GSI Scientific Report 2013*, in print (GSI Library, 2014).
- [84] G. Weber, C. Hahn, A. Paz, and R. Märtin, in *GSI Scientific Report 2012* (GSI Library, 2013).
- [85] Y. T. Li, X. H. Yuan, M. H. Xu, Z. Y. Zheng, Z. M. Sheng, M. Chen, Y. Y. Ma, W. X. Liang, Q. Z. Yu, Y. Zhang, F. Liu, Z. H. Wang, Z. Y. Wei, W. Zhao, Z. Jin, and J. Zhang, *Phys. Rev. Lett.* **96**, 165003 (2006).

Statement of Authorship

I declare, that I have independently written the work presented here, and I have not used any help other than from the stated sources and resources.

I give consent to this copy of my thesis, when deposited in the Thuringian University and State Library, being made available for public use and photocopying.

Hao Ding
Jena,